Coastal Engineering 171 (2022) 104057

Contents lists available at ScienceDirect

Coastal Engineering

journal homepage: www.elsevier.com/locate/coastaleng

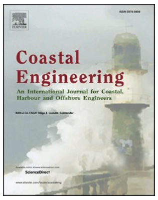

Accounting for uncertainties in compound flood hazard assessment: The value of data assimilation

David F. Muñoz[a,b,*], Peyman Abbaszadeh[a,b], Hamed Moftakhari[a,b], Hamid Moradkhani[a,b]

[a] Department of Civil, Construction and Environmental Engineering, The University of Alabama, Tuscaloosa, AL, 35487, United States
[b] Center for Complex Hydrosystems Research, The University of Alabama, Tuscaloosa, AL, 35487, United States

ARTICLE INFO

Keywords:
Compound flooding
Data assimilation
Ensemble kalman filter
Flood forecasting
Hurricanes

ABSTRACT

Compound flood hazard assessment (CFHA) and modeling are prone to various sources of uncertainty including model structure, model parameters, input/forcing data, and those associated with nonlinear interactions among flood drivers. Data assimilation (DA) is an efficient method that helps quantify and reduce uncertainty in many hydrological applications and has proven to be effective in water level (WL) predictions and/or flood forecasts. However, research to date has not yet explored the benefits of DA in coastal to inland transition zones where pluvial, fluvial, and coastal flood drivers interact. Here, we present a DA scheme consisting of the Ensemble Kalman Filter technique and hydrodynamic modeling to provide (i) reliable WL predictions and (ii) accurate (near real-time) flood hazard maps within a 6 h-assimilation cycle. The DA scheme is tested on two well-known compound flood events and study sites in the United States, namely Hurricane Harvey for Galveston Bay and Hurricane Sandy for Delaware Bay. WL predictions and compound flood hazard maps are validated against observational data collected from coastal and inland gauge stations and high-water marks obtained from the U.S. Geological Survey, respectively. We show that DA is an effective method that accounts for all sources of uncertainty, reduces errors in peak WL estimates (up to 0.55 m) and mean absolute bias in CFHA (up to 40%). We conclude that, regardless of the dominant fluvial/pluvial or coastal drivers, DA can improve CFHAs in low-lying areas including coastal to inland transition zones.

1. Introduction

Compound events result from a combination of multiple drivers and/or hazards that contributes to societal or environmental risks (Zscheischler et al., 2020). During these events, spatiotemporal coincidence/succession of multiple (non-) extreme hazards and the associated nonlinear interactions among physical processes (e.g., oceanic, hydrological, and meteorological) can lead to larger impacts than those from isolated hazards (AghaKouchak et al., 2018; Leonard et al., 2014). Such nonlinear interactions along with sea level rise and anthropogenic activities (e.g., land cover land use change, water extraction, and climate change) may escalate flood risk globally and impact ~190 million people currently living below high tide lines (Kulp and Strauss, 2019). Over the past years, compound flooding (CF) has been studied with statistical, physically-based, or combined approaches improving compound flood hazard assessments (CFHAs) at different spatial scales. In this section, we present an overview of current approaches for CFHA, identify the associated sources of uncertainty, and describe data assimilation (DA) techniques used to improve forecasts from hydrological, meteorological, and oceanic models. In Section 2, we introduce the study sites, indicate available (open-source) data, and develop a DA scheme aimed at improving water level prediction and CFHA in coastal to inland transition zones. Then, we discuss the results of the proposed scheme in Section 3 and further provide conclusions and remarks in Section 4.

1.1. *Compound flood hazard assessment*

Statistical approaches for CFHA help characterize the joint occurrence of extreme events via multivariate analyses (Bensi et al., 2020; Sadegh et al., 2018; Salvadori et al., 2016), hence allowing researchers to conduct assessments at different spatial scales (Hendry et al., 2019; Wahl et al., 2015; Ward et al., 2018). However, these approaches require observational data from gauge stations having a considerable length of records to account for uncertainties when characterizing flood hazards at low frequencies or long return periods (e.g., 25, 50, and 100 years).

---

[*] Corresponding author. Department of Civil, Construction and Environmental Engineering, The University of Alabama, Tuscaloosa, AL 35487, United States.
E-mail address: dfmunoz1@ua.edu (D.F. Muñoz).

https://doi.org/10.1016/j.coastaleng.2021.104057
Received 21 June 2021; Received in revised form 9 November 2021; Accepted 20 November 2021

Moreover, even if data are available for several years, these approaches may not necessarily lead to identical CFHAs as gauge (point-based) measurements cannot fully capture the spatiotemporal patterns of CF (Ghanbari et al., 2021; Moftakhari et al., 2017; Nasr et al., 2021). In contrast, physically-based approaches allow for simulating CF and generating flood maps over a user-defined model domain for a given compound event (Valle-Levinson et al., 2020; Ye et al., 2021). Particularly, two-dimensional (2D) hydrodynamic models require a detailed mesh resolution (or cell size) to ensure a correct representation of relevant topographic and bathymetric (topobathy) features and accurately simulate water level (WL) dynamics (Bilskie and Hagen, 2013). Therefore, a series of hydrodynamic models have been developed to solve the continuity and momentum equations (Equations (1)–(3), in section 2.3) in 2D depth-average mode (e.g., ADCIRC, Delft3D-FM, HEC-RAS, ROMS, etc.) and subsequently conduct CFHAs. However, these approaches are computationally intensive despite the growing access to powerful and low-cost computational resources.

Linking statistical and physically-based approaches can alleviate computational burden since hydrodynamic simulations and/or CFHAs focus on the most likely boundary (forcing) conditions given the correlation structure of hazard drivers and desired return period (Moftakhari et al., 2019; Muñoz et al., 2020; Serafin et al., 2019). Despite the advantages and limitations of both statistical and physically-based approaches, a thorough CFHA should also account for uncertainties derived from boundary conditions (BCs) and/or validation data, model parameters, and model structure (Moradkhani et al., 2018; Nearing et al., 2016; Wu et al., 2020). These sources of uncertainty, when not accounted for, can significantly affect the accuracy of inundation depth, flood extent, and velocity maps in hydrological and coastal systems (Parodi et al., 2020; Saleh et al., 2017; Wechsler, 2007).

1.2. *Uncertainty sources*

Uncertainty from BCs in compound flood modeling is associated with the initial state and forcing data of the system. The initial state is affected by the uncertainty of topobathy data including an inadequate representation of flood-protection infrastructure in digital elevation models (DEMs) (e.g., seawalls, levees, and coastal barriers) (Gallien et al., 2018; Sanders and Schubert, 2019). In coastal systems, wetland coverage is a well-known source of vertical bias especially in light detection and ranging-derived DEMs where overestimation of true topographic elevation can be as high as 0.65 m (Alizad et al., 2018; Medeiros et al., 2015). Uncertainty of bathymetric data directly affects velocity and current speed magnitudes, which in turn alters complex processes such as sedimentation, salinization, and mixing in rivers and estuaries (Cea and French, 2012). Likewise, forcing data (or BCs) and observations are other sources of uncertainty that can potentially affect the accuracy of CFHA. These uncertainties are often estimated a priori (Moradkhani et al., 2018) or ignored depending on the quality of the data source. For example, observation errors from WL stations of the National Oceanic and Atmospheric Administration (NOAA) are in the order of millimeters (1 mm) (Asher et al., 2019) whereas discharge measurements from U.S. Geological Survey (USGS) stations can range from excellent to poor quality, i.e., data within 2% and >8% of actual flow, respectively (USGS, 2011).

Another important source of uncertainty is derived from model parameters including roughness coefficient, wind-drag, eddy viscosity and diffusivity, and other physically-related coefficients that control the dynamics of coastal processes. Among those parameters, the Manning's roughness coefficient is known to alter WL and/or inundation dynamics and therefore requires a robust calibration based on land cover and land use maps. When such maps are not available at the desired resolution, alternatively, land cover maps derived from remote sensing data can be used (Muñoz et al., 2021a; Potapov et al., 2020). This in turn aims at improving traditional approaches that rely on a single roughness coefficient for estuarine, riverine and floodplain areas (Liu et al., 2018; Ye et al., 2020). Lastly, uncertainty from model structure (or process uncertainty) refers to limitations and a priori assumptions of underlying processes simulated in physically-based models (Moradkhani et al., 2018; Nearing et al., 2016). Models are themselves uncertain as they discretize oceanic, hydrological, and meteorological processes to make them suitable for numerical evaluation. Moreover, when using model coupling frameworks to provide CFHAs, the uncertainty of modeling processes propagates through the coupled models in series (Hasan Tanim and Goharian, 2021; Joyce et al., 2018). This in turn requires advanced statistical methods to account for model's uncertainty and reduce systematic errors.

1.3. *Accounting for uncertainties using data assimilation*

The aforementioned uncertainties can be accounted for with sequential DA procedures. The purpose of DA is to combine information from model states with in-situ and/or remotely-sensed observations for a better forecast of the fields of interest (Moradkhani, 2008). DA has been widely used to estimate uncertainties and improve forecasts from hydrological (Abbaszadeh et al., 2020; Pathiraja et al., 2018), meteorological (Houtekamer and Zhang, 2016; Navon, 2009) and oceanic models (Bertino et al., 2003; Ghil and Malanotte-Rizzoli, 1991). In contrast, relatively few studies have successfully implemented DA techniques with coastal-ocean models to reduce uncertainties in storm-surge forecasting and coastal inundation. Heemink (1986) conducted one of the pioneer studies for storm-surge prediction using Kalman filtering (Kalman, 1960). Later on, Verlaan and Heemink (1997) and Cañizares et al. (1998) proposed an approximation of the Kalman Filter algorithm via reduced-rank square-root filter to forecast tidal flows and initialize storm-surge models, respectively. Madsen and Cañizares (1999) evaluated the performance of extended and Ensemble Kalman Filter (EnKF) methods for assimilation of WL measurements in an idealized bay region. They pointed out the ability of both methods to efficiently correct model states given a suitable number of leading eigenvalues and ensemble size, and further recommend EnKF for assimilating coastal WLs due to highly nonlinear dynamics that arise in flooding and drying of tidal areas.

More recent studies in storm-surge modeling have proposed alternatives of the Kalman filter algorithm to better propagate the error covariance and reduce the computational burden of stochastic realizations of coastal ocean models. Among those studies, Mayo et al. (2014) used the singular evolutive interpolated Kalman Filter to estimate roughness (Manning's) coefficients by assimilating water elevation data of an idealized inlet and a coarser representation of Galveston Bay, TX. They estimated bed roughness for non-extreme events and/or under typical weather conditions where astronomical tides are the dominant forcing condition. Likewise, Asher et al. (2019) developed an optimal interpolation-based DA scheme to correct WL residuals, i.e., observed minus simulated WLs, of Hurricane Matthew (Oct/2016) along the southeast Atlantic coasts of the U.S. Asher et al. (2019) concluded that WL residuals are associated with 'unresolved drivers' resulting from additional physical processes (e.g., steric variations, baroclinicity, major ocean currents, etc.) that are not fully resolved by the continuity and momentum equations, i.e., model structural error.

Although these studies implemented DA to estimate model parameters and correct WLs at the coastal-ocean interface, to the best of our knowledge, there are no studies that explore the benefits of DA for CFHA in coastal to inland transition zones where pluvial, fluvial, and coastal processes are all of paramount importance (Bilskie and Hagen, 2018). To address this research gap, we integrate hydrodynamic modeling (Delft3D-FM) with the EnKF technique for correcting peak water surface elevation and improving the accuracy of compound flood maps for two well-known extreme events: (i) Hurricane Sandy that affected Delaware Bay, DE in October 2012, and (ii) Hurricane Harvey that hit twice Galveston Bay, TX in August 2017. Integration of data assimilation and hydrodynamic modeling can enhance stakeholder engagement, assist disaster coordinators and decision makers in risk-informed planning and efficient emergency responding (Sanders et al., 2020).

2. Materials and method

2.1. Study area

We select two strategic study sites with unique characteristics and corresponding compound flood events to evaluate the feasibility of DA in CFHA. Galveston Bay (G-Bay) is an inlet of the Gulf of Mexico and the seventh-largest estuary in the United States (Fig. 1a). G-Bay is a relatively shallow water body of 2 m depth, 56 km length and 31 km width that comprises a total area of 1 600 km^2 approximately (Huang et al., 2021; Sebastian et al., 2014, 2019). Freshwater runoff input to the Bay comes from the Buffalo Bayou River (Houston Ship Channel) including several streams that join the river in Houston city. The annual average discharge measured at Buffalo Bayou station (USGS 08074000) is 50 m^3/s approximately. The San Jacinto River is another important freshwater source that connects Lake Houston to G-Bay. The Lake Houston dam (and spillway on top) can release a maximum flow of 283 m^3/s through its gates. An important fact of Hurricane Harvey is that the flow exceeded the dam's capacity, and as a result, a 3.35 m column of water was flowing over the 963 m long spillway (https://reduceflooding.com/2019/11/13/aerial-photos-of-lake-houston-dam-dramatize-need-for-more-gates/). Tides in G-Bay are mixed based on the form factor (Pugh and Woodworth, 2014) and so characterized by the lunar diurnal constituent (K_1) and principal lunar semidiurnal constituent (M_2) with tidal amplitudes of 0.15 m and 0.11 m, respectively. Ten stations from the NOAA and USGS provide water surface level for model calibration (blue squares) comprising the Bay and Houston city downtown (orange polygon). According to official reports of NOAA and the National Hurricane Center, Hurricane Harvey (August 2017) was responsible for one of the most catastrophic flooding events in the Unites States. Harvey made landfall twice in Texas leading to extremely high cumulative rainfall of more than 1 524 mm over southeastern Texas, and subsequent pluvial flooding with up to 3 m of water above ground level (Blake and Zelinsky, 2018).

Delaware Bay (D-Bay) is a natural state border of New Jersey and Delaware in the east coast of the United States (Fig. 1b). D-Bay is a diamond-shape water body of 210 km length and 45 km width (18 km at the mouth) that comprises a total area of 2030 km^2 approximately (Whitney and Garvine, 2006). The Delaware River (USGS 01463500) and Schuylkill River (USGS 01474500) are two main freshwater runoff inputs to the Bay and have an annual average discharge of 340 m^3/s and 82 m^3/s, respectively. D-Bay has an average bathymetry of 7 m approximately and counts with a deep channel (>28 m) along its longitudinal axis designed for navigational purposes. Tides in the lower part of D-Bay are semidiurnal with M_2 tidal amplitudes of 0.75 m. Ten stations from the NOAA and USGS are considered for model calibration (blue squares) comprising D-Bay and its lateral floodplains (orange polygon). The Atlantic Hurricane season has affected D-Bay since 1749 with more than hundred tropical cyclones producing extreme storm surges, strong winds and heavy rainfall (Salehi, 2018). Among the major historical hurricanes that impacted D-Bay (NOAA-NHC, 2020), Hurricane Sandy (October 2012) resulted from a combination of extreme storm surge and moderate rainfall causing pluvial flooding at the coast with 1.50 m of water above ground level in Delaware City (Blake et al., 2013).

2.2. Data availability

We use publicly available data to develop a hydrodynamic model of each study site and then validate our results with respect to ground-truth and satellite-based data. Topobathy data are obtained from coastal

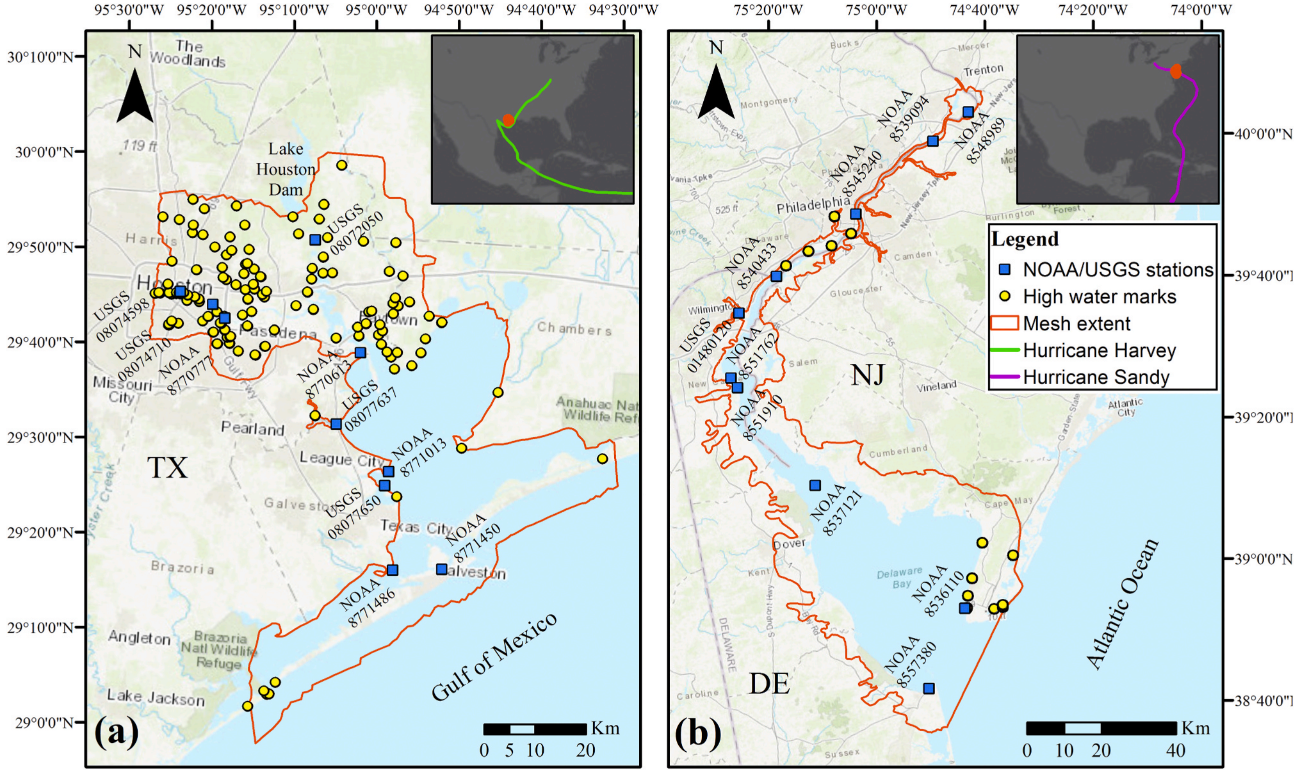

Fig. 1. Map of the study sites (orange polygons) including available NOAA and USGS stations (blue squares) for model calibration and compound flood hazard assessment with data assimilation. USGS high water marks (yellow circles) provide inundation depths within the mesh extent of (a) Galveston Bay, TX and (b) Delaware Bay, DE. Hurricane's best track of Harvey (green line) and Sandy (purple line) are shown in the top right corners, respectively. (For interpretation of the references to colour in this figure legend, the reader is referred to the Web version of this article.)

DEMs of the NOAA's Data Access Viewer (https://coast.noaa.gov/). The data is referenced to the North American Vertical Datum 1988 (NAVD88) and have a spatial resolution of 1 m. Manning's roughness coefficients for D-Bay and G-Bay are initially derived from the 2011 and 2016 National Land Cover Database (NLCD) maps, respectively (https://www.mrlc.gov/data). The selected NLCD maps have a 30 m spatial resolution with 16 land cover classes representing pre-flood conditions. For simplicity, the classes were re-grouped into a more general classification to avoid unnecessary specificity in model calibration (see section 2.3.2 for details).

Time-series of observed hourly WL are obtained from NOAA's Tide & Currents portal (https://tidesandcurrents.noaa.gov/) and are used as downstream BCs at selected stations as well as calibration data for the hydrodynamic models. In addition, we use time-series of hourly river discharge from the USGS portal (https://maps.waterdata.usgs.gov/mapper/) as upstream BCs at selected stations. Some USGS stations with available WL records are also considered for model calibration (Fig. 1). Likewise, post-flood high-water marks (HWMs) from the USGS indicating inundation depth at several locations of G-Bay and D-Bay are available in the Flood Event Viewer website (https://stn.wim.usgs.gov/fev/). Local wind (10 m height), sea level pressure and rainfall data are obtained from the ERA5 reanalysis dataset (https://www.ecmwf.int/en/forecasts/datasets/reanalysis-datasets/era5). The dataset consists of gridded hourly data with a spatial resolution of 30 km.

2.3. *Model configuration*

Hydrodynamic models of G-Bay and D-Bay are developed with the 2021 Delft3D-FM suite package in 2D (depth-averaged) mode (Roelvink and Van Banning, 1995). The models use an unstructured finite volume grid to solve the depth-averaged continuity and momentum equations (Equations (1)–(3)) under the assumption that vertical length scales are significantly smaller than the horizontal ones (Lesser et al., 2004). Delft3D-FM can simulate complex riverine, estuarine and intertidal flat hydrodynamics and account for nonlinear interactions of river flow, rainfall, storm-surge, wind, etc. (Deltares, 2021). Moreover, the model package has been used in several CF studies at local and regional scale with satisfactory results (Bevacqua et al., 2019; Muis et al., 2019; Salehi, 2018).

$$\frac{\partial \zeta}{\partial t}+\frac{\partial (h+\zeta)u}{\partial x}+\frac{\partial (h+\zeta)v}{\partial y}=0 \qquad (1)$$

$$\frac{\partial u}{\partial t}+u\frac{\partial u}{\partial x}+v\frac{\partial u}{\partial y}-fv=-\frac{1}{\rho_0}\frac{\partial p}{\partial x}-g\frac{\partial \zeta}{\partial x}+\nu_V\left|\frac{\partial^2 u}{\partial x^2}+\frac{\partial^2 u}{\partial y^2}\right|+\frac{\tau_b+\tau_w}{\rho_0}+M_x \qquad (2)$$

$$\frac{\partial v}{\partial t}+u\frac{\partial v}{\partial x}+v\frac{\partial v}{\partial y}+fu=-\frac{1}{\rho_0}\frac{\partial p}{\partial y}-g\frac{\partial \zeta}{\partial y}+\nu_V\left|\frac{\partial^2 v}{\partial x^2}+\frac{\partial^2 v}{\partial y^2}\right|+\frac{\tau_b+\tau_w}{\rho_0}+M_y \qquad (3)$$

where ζ is water surface elevation (above still water), t is time, h is water depth (below horizontal datum or still water), and u and v are the 2D depth-averaged velocities in x and y directions, respectively. f is the Coriolis parameter, τ_b is bottom friction, τ_w is wind friction acting at the free surface, ρ_0 is the constant water density, p is the atmospheric (sea level) pressure, g is the acceleration of gravity, ν_V is the vertical eddy viscosity coefficient, and M_x and M_y represent the contributions due to external sources or sinks of momentum (e.g., discharge or withdrawal of water).

2.3.1. *Model setup*

The G-Bay model has a varying cell-size spatial resolution ranging from 20 m in Houston city and the navigational channel up to 2 km in the Gulf of Mexico. The unstructured mesh comprises key features of the system such as the Houston Ship Channel, lateral floodplains, wetlands, and natural parks located downstream the Lake Houston Dam (Fig. 2a). The mesh at Houston city is limited by several discharge BCs including Whiteoak Bayou (USGS 08074500), Buffalo Bayou (USGS 08073700), Brays Bayous (USGS 08075000), and Sims Bayou (USGS 08075500). The Lake Houston Dam limits the mesh at the northern side where the sum of all upstream freshwater input is used as BC. Clear Creek (USGS 08077600) and the Trinity River (USGS 08067252) limit the mesh at the western and eastern side, respectively. For simplicity, three downstream BCs at the ocean boundary namely San Luis Pass (NOAA 8771972),

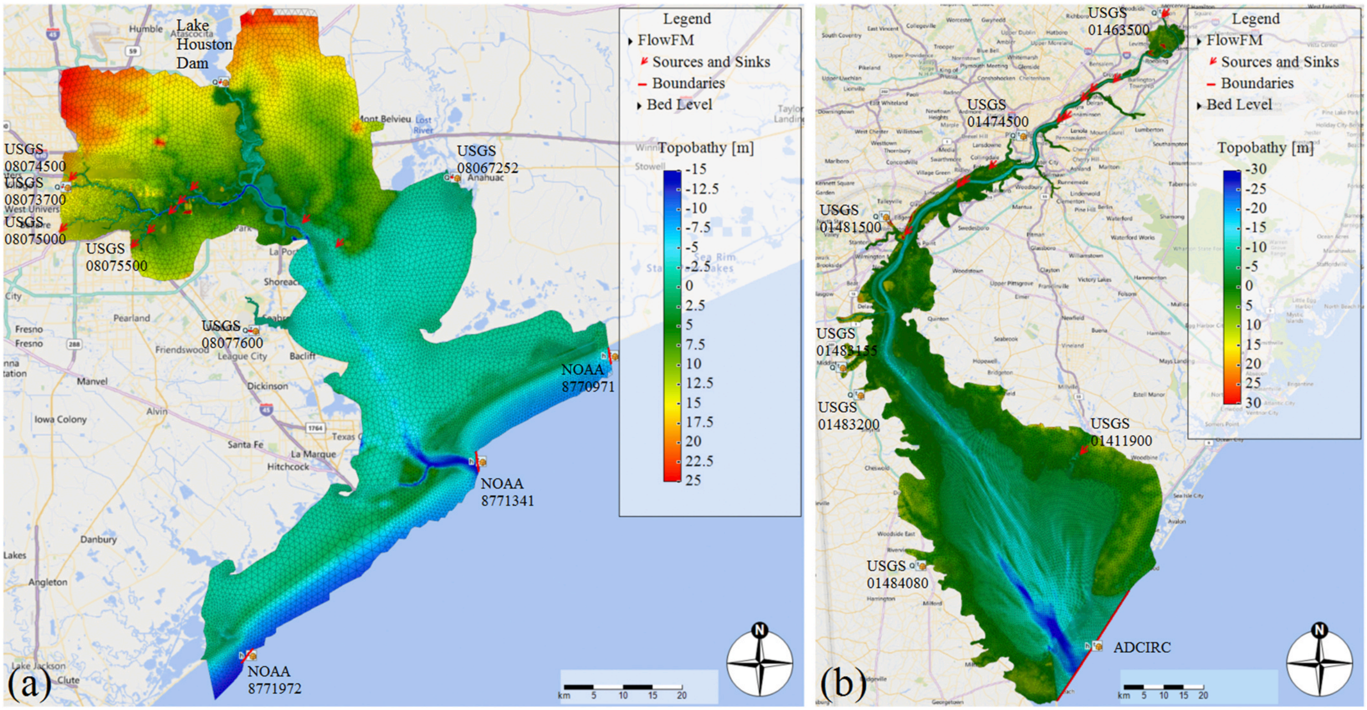

Fig. 2. Model domain, USGS/NOAA boundary conditions, and topobathy data (NAVD88 datum) interpolated over the unstructured mesh of (a) Galveston Bay, TX, and (b) Delaware Bay, DE.

Galveston Bay Entrance (NOAA 8771341), and Rollover Pass (NOAA 8770971) provide coastal WLs at the outlet of the Bay.

The D-Bay model has a cell-size spatial resolution of 20 m in urban areas and around the navigational channel that connects the Bay with the Delaware River (Fig. 2b). A coarser resolution up to 1.4 km is used in the Atlantic Ocean and in some parts of the Bay with relatively large water depths. The unstructured mesh cover wetland regions, small streams and lateral floodplains in Delaware and New Jersey (Fig. 2b). Discharge BCs in the upstream part of the Bay include the Delaware River (USGS 01463500), Schuylkill River (USGS 01474500), Brandywine Creek (USGS 01481500), Silver Lake tributary (USGS 01483155) and Blackbird Creek (USGS 01483200). The mesh is also limited at the western and eastern side by the Murderkill River (USGS 01484080) and Maurice River (USGS 0 1411900), respectively. In absence of a representative gauge station at the bay-ocean boundary, coastal WLs are derived from model simulations of the Advanced Circulation (ADCIRC) model. These time-series data were used in a similar flood study involving the Delaware Bay basin and Hurricane Sandy (Bakhtyar et al., 2020).

We use local wind, sea level pressure, and precipitation data obtained from the ERA5 reanalysis dataset as additional forcing into the model. Likewise, we correct vertical bias in wetland areas of G-Bay and D-Bay prior interpolation over the unstructured mesh. For this, we use a previously developed 'DEM-correction' tool that adjust surface elevation in coastal wetlands based on 'emergent herbaceous' wetland coverage of the NLCD (Muñoz et al., 2019). The tool modifies an existing DEM through linear elevation adjustment and site-specific parameters (Alizad et al., 2018), and helps reduce uncertainty in compound flood and velocity maps derived from hydrodynamic simulations (Muñoz et al., 2020).

2.3.2. Model calibration

We calibrate roughness values based on the 2011 and 2016 NLCD maps of D-Bay and G-Bay, respectively, as they contain land cover distributions prior to any effects of hurricane-induced flooding such as wetland loss, shoreline erosion, and sediment deposition (Morton and Barras, 2011). It is important to note that here the goal of model calibration is to estimate the best possible model parameters and provide reasonable initial state estimates of the system (e.g., surface WL and flow velocities) used for further ensemble-based model simulations (see section 2.4.3 for details). For this, we regrouped and refined the original NLCD classes into five main categories as follows: open water, riverine water, navigational (or dredged) areas, coastal wetlands, and urban areas (Fig. 3). The remaining land cover classes of the NLCD map (e.g., crops, pasture, forest, etc.) are left with recommended roughness values due to their negligible effect on flood dynamics (dry areas).

A common approach for hydrodynamic model calibration consists of multiple runs with randomly sampled Manning's roughness values (e.g., Monte Carlo approach) with the objective of: (i) minimizing the root mean square error (RMSE) between observed and simulated WLs, and (ii) maximizing their correlation. However, those 'calibrated' values may not be the optimal ones due to Monte Carlo the sampling procedure. Another alternative for calibration is the Latin Hypercube Sampling (LHS) technique that has been used for uncertainty propagation in complex systems and models (Cea and French, 2012; Iman et al., 1981). LHS results in a denser stratification over the range of each sampled parameter as compared to random sampling. Furthermore, the advantage of LHS over Monte Carlo is that the former technique leads to more stable results, i.e., close to the true probability density function of the parameter, and facilitates the identification of interactions among multiple parameters (Helton and Davis, 2003).

We therefore sample roughness values with the LHS technique and use pre-defined lower and upper limits for each land cover category (Table 1). The range of Manning's roughness values is derived from

Table 1
Range of Manning's roughness values used for calibration of Delaware Bay and Galveston Bay models.

Land cover category	Lower limit	Upper limit	G-Bay[a]	D-Bay[a]
Open water	0.005	0.035	0.015	0.021
Riverine water	0.010	0.150	0.037	0.028
Navigation areas	0.010	0.200	0.011	0.012
Coastal wetlands	0.025	0.200	0.051	0.159
Urban areas	0.020	0.070	0.030	0.021

[a] Optimal (calibrated) roughness values.

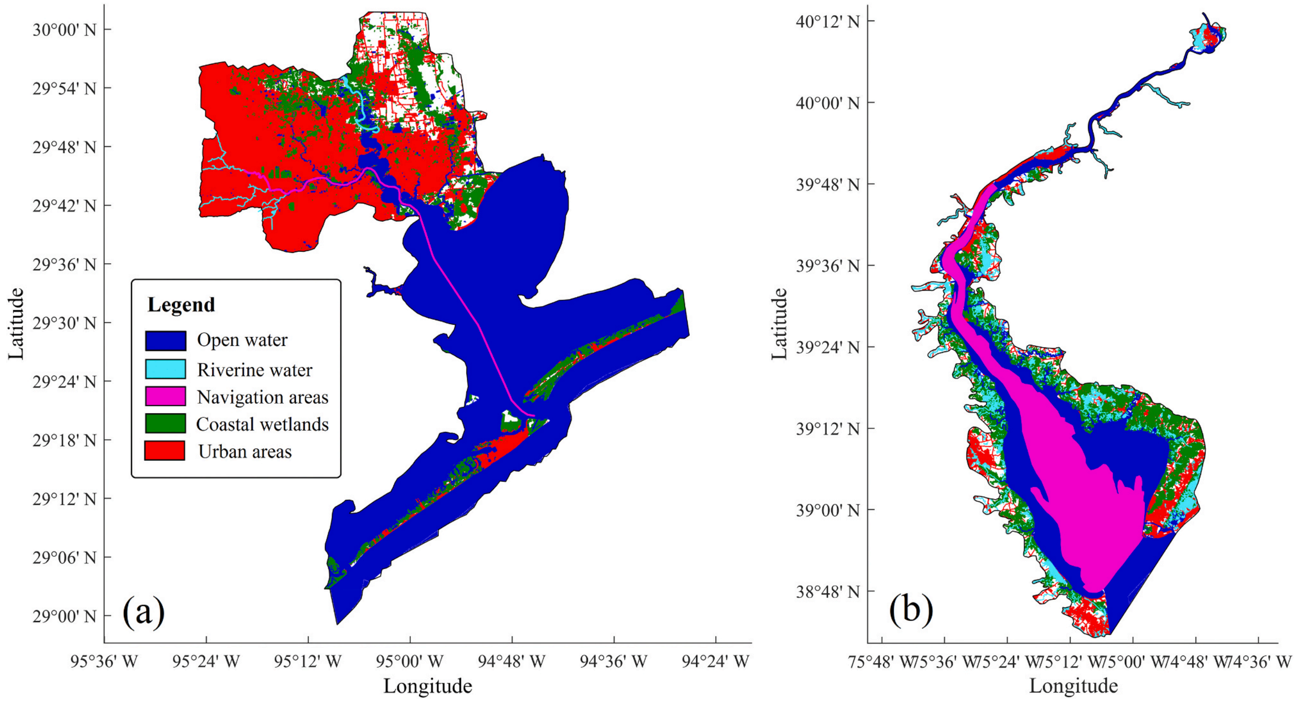

Fig. 3. Land cover categories used for model calibration via the Latin Hypercube Sampling (LHS) technique in (a) Galveston Bay, TX and (b) Delaware Bay, DE.

pertinent literature including hydrodynamic and open channel flow studies (Arcement and Schneider, 1989; Chow, 1959; Liu et al., 2018). Model runs start on August 5, 2017 and October 11, 2012 for G-Bay and D-Bay, respectively, and ensure WL variability during high and low tides in the system, i.e., spring-neap tidal cycle (Pugh and Woodworth, 2014). We intentionally consider extreme WLs of Hurricane Harvey and Sandy in the calibration process to prove the benefits of DA in CFHA even with a rigorously calibrated model.

2.3.3. Evaluation metrics

We compare observed and simulated WLs using the Taylor diagram (Taylor, 2001) as proposed in hydrological and coastal studies (Abbaszadeh et al., 2018; DeChant and Moradkhani, 2012; Muñoz et al., 2020). The diagram combines three performance measures to evaluate the goodness of fit between two time series: i) the Pearson's correlation coefficient (R^2) that measures the strength (and direction) of a linear relationship between the time series, ranging from 0 (poor) to 1 (perfect match), ii) the normalized root mean square difference (RMSD) that quantifies the similarity between the time series and ranges from 0 (perfect analogy) to ∞ (total dissimilarity), and iii) the standard deviation ratio (or ratio of variances) that quantifies the relative amplitude of variation between the time series; where the smaller the variation the closer SDR to 1. Likewise, we use additional deterministic and probabilistic metrics to provide a robust analysis of model calibration and the assimilation process. Those metrics are the Nash-Sutcliffe efficiency (NSE) ranging from 0 to 1 (Nash and Sutcliffe, 1970), the Kling-Gupta efficiency (KGE) with values between -∞ and 1 where efficiency of 1 indicates a perfect match (Gupta et al., 2009), and the mean absolute bias (MAB) that quantifies the bias of the simulated variable with respect to the observation data. In MAB, a value of 0 suggests an absence of bias in model simulations. Lastly, reliability (RL) is a probabilistic metric that quantifies the statistical consistency between a time-varying variable and the corresponding distribution (Renard et al., 2010). RL ranges from 0 (poor) to 1 (perfect match) between the predictive Q-Q plot and the theoretical quantile of uniform distribution (U [0,1]). For the readers' convenience, all pertinent equations are included in the appendix (Table A1).

2.4. Data assimilation

DA consists of the application of Bayes' theorem to probabilistically condition model states on observations; and ultimately forecast the state of a system based on the knowledge of the initial state (Moradkhani et al., 2018). We define WL in coastal to inland transition zones as the model state (Equation (4)) and condition simulated WLs from hydrodynamic modeling to the corresponding observation at the USGS and NOAA stations (Equation (5)). Hereinafter, we follow the nomenclature proposed in Moradkhani et al. (2005) to define all pertinent variables.

$$x_{t+1} = f(x_t, u_t, \theta) + \omega_t; \quad \omega_t \sim \dot{N}\left(0, \Sigma^x_t\right) \tag{4}$$

$$\hat{y}_{t+1} = h(x_{t+1}, \theta) + \nu_{t+1}; \quad \nu_{t+1} \sim \dot{N}(0, \Sigma^y_{t+1}) \tag{5}$$

where x_t, $\hat{y}_t$, and u_t are model state, model prediction, and forcing data vectors at the current time-step t, respectively. $f(.)$ is the generalized nonlinear state-transfer function (or forward operator) whereas $h(.)$ is the observation operator that translates model states into observation space. ω_{t+1} and ν_{t+1} are additive noise terms (e.g., stochastic or random error) representing uncertainties from model structure and observation data, respectively. Both uncertainties are assumed to be independent of each other and derived from a normal ($\dot{N}$) or Gaussian distribution with zero mean and covariances Σ^x_t and Σ^y_{t+1} (Moradkhani et al., 2005). θ is a time-invariant parameter vector that represents (calibrated) spatially varying Manning's roughness values (Table 1).

For simplicity, we assume that a robust calibration of spatially varying θ-values in coastal to inland transition zones (see section 2.3.2) in addition to accurate topobathy data (see section 2.2) can lead to reasonable WL estimates without requiring a sequential update or adjustment through time. Moreover, compound effects of flood drivers have a relatively short duration (e.g., lag times up to 7 days) that might not significantly alter the previously calibrated roughness values (Klerk et al., 2015; Ward et al., 2018).

2.4.1. Ensemble Kalman Filter technique

The EnKF uses a recursive algorithm that process a pre-defined set of ensemble model states (Equation (6)) and allows for constructing time-evolving probability density functions with the associated error covariance matrix (Moradkhani et al., 2005). Those functions are sequentially adjusted in the algorithm to match observations, which must be treated as a random variable (Burgers et al., 1998). This in turn prevents that the updated ensemble results in unrealistic (too low) variances (Equation (7)). Similarly, uncertainty from forcing data is often derived from stochastic perturbations with a Gaussian error (Equation (8)). However, in low-lying areas, CF is dominated by extreme coastal WLs (e.g., storm surge) that are better characterized by the General Extreme Value (*GEV*) distribution (Muis et al., 2019; Wahl et al., 2017).

$$x^{i-}_{t+1} = f\left(x^{i+}_t, u^i_t, \theta\right) + \omega^i_t; \quad \omega^i_t \sim \dot{N}\left(0, \Sigma^x_t\right) \tag{6}$$

$$y^i_{t+1} = y_{t+1} + \nu^i_{t+1}; \quad \nu^i_{t+1} \sim \dot{N}(0, \Sigma^y_{t+1}) \tag{7}$$

$$u^i_t = u_t + \zeta^i_t; \quad \zeta^i_t \sim \dot{N}\left(0, \Sigma^u_t\right) \tag{8}$$

where $i = 1, 2, 3 \ldots n$-ensemble members. x^{i-}_{t+1} and x^{i+}_{t+1} are the ith forecast (prior) ensemble member at time $t+1$ and the ith updated (posterior) ensemble member at time t, respectively. y^i_{t+1} is the ith observation replicate whose mean value is the actual observation and noise term derived from a $\dot{N}$ distribution. Similarly, u^i_t is the ith forcing replicate with Gaussian noise (ζ^i_t) of zero mean and covariance Σ^u_t (Moradkhani et al., 2005).

We perturb forcing data using the *GEV* distribution for downstream BCs (coastal WL) and the $\dot{N}$ distribution for upstream BCs (river discharge) accordingly. Regarding the *GEV* distribution, we conveniently select NOAA stations having long records to ensure a proper characterization of extremes. Those stations are Galveston Pier 21, TX (NOAA – 8771450) and Lewes, NJ (NOAA – 8557380) as they have been collecting hourly WL data since 1904 and 1919, respectively. The error covariance matrix associated with the state forecast estimate (Equation (9)) and observation forecast (Equation (10)) is calculated after each round of ensemble model simulations. Subsequently, the Kalman gain (Equation (11)) is estimated with the forecast cross-covariance matrix of the state variables (Equation (12)) and the forecast error covariance matrix of the observation forecast (Equation (13)).

$$E\left[x^{i-}_{t+1}\right] = \frac{1}{N}\sum_{i=1}^{N} x^{i-}_{t+1} \tag{9}$$

$$E\left[\hat{y}^i_{t+1}\right] = \frac{1}{N}\sum_{i=1}^{N} \hat{y}^i_{t+1} \tag{10}$$

$$K_{t+1} = \Sigma^{xy-}_{t+1}\left(\Sigma^{yy-}_{t+1} + \Sigma^y_{t+1}\right)^{-1} \tag{11}$$

$$\Sigma^{xy-}_{t+1} = E\left[\left(x^{i-}_{t+1} - E\left[x^{i-}_{t+1}\right]\right)\left(\hat{y}^i_{t+1} - E\left[\hat{y}^i_{t+1}\right]\right)^T\right] = \ldots$$

$$\ldots \frac{1}{N}\sum_{i=1}^{N}\left\{\left(x^{i-}_{t+1} - E\left[x^{i-}_{t+1}\right]\right)\left(\hat{y}^i_{t+1} - E\left[\hat{y}^i_{t+1}\right]\right)^T\right\} \tag{12}$$

$$\Sigma^{yy-}_{t+1} = E\left[\left(\hat{y}^i_{t+1} - E\left[\hat{y}^i_{t+1}\right]\right)\left(\hat{y}^i_{t+1} - E\left[\hat{y}^i_{t+1}\right]\right)^T\right] = \ldots$$

$$\dots \frac{1}{N}\sum_{i=1}^{N}\left\{\left(\widehat{y}_{t+1}^{i}-E\left[\widehat{y}_{t+1}^{i}\right]\right)\left(\widehat{y}_{t+1}^{i}-E\left[\widehat{y}_{t+1}^{i}\right]\right)^{T}\right\} \tag{13}$$

Equations (9)–(13) follow the standard Kalman Filter formulation except that the model covariances are directly estimated with the ensemble members. In addition, these set of equations simplify the updating process as there is no need of linearization of the model (Moradkhani et al., 2018). Lastly, the ensemble members are updated as follows:

$$x_{t+1}^{i+}=x_{t+1}^{i-}+K_{t+1}\left(y_{t+1}^{i}-\widehat{y}_{t+1}^{i}\right) \tag{14}$$

2.4.2. *Mass and force balance closure*

A well-known limitation of the EnKF is that this technique alters the mass water balance (or continuity equation) when adding or subtracting water into/from the system to update model states (Abbaszadeh et al., 2019; DeChant and Moradkhani, 2012; Matgen et al., 2010). Likewise, such an update (or correction) of surface WL will not last enough in coastal systems due to a rapid barotropic adjustment in the velocity field (Asher et al., 2019; Valle-Levinson, 2010). A possible solution that might help achieve an adequate mass and force balance closure of the system consists in a simultaneous update of forcing data and model states in the continuity (Eq. (1)) and momentum equations (Eqs. (2) and (3)), respectively. Following the approach of Asher et al. (2019), we introduce a fictitious force term in the momentum equation to match the WL correction accordingly. This force is derived from the inverse barometer relationship (Equation (15)) that relates any changes in atmospheric pressure (Δp) to the corresponding changes in surface WL ($\Delta\zeta$).

$$p=p_a+\Delta p=\ p_a-\rho_0\, g\, \Delta\zeta \tag{15}$$

where p_a is the actual pressure and Δp is referred as the pseudo atmospheric pressure.

Substituting this expression into the momentum equations (Eqs. (2) and (3)), the so-called pseudo atmospheric pressure allows the WL correction to propagate over the other equation terms (Equations (16) and (17)).

$$\frac{\partial u}{\partial t}+u\frac{\partial u}{\partial x}+v\frac{\partial u}{\partial y}-fv=-\frac{1}{\rho_0}\frac{\partial p_a}{\partial x}-g\frac{\partial(\zeta-\Delta\zeta)}{\partial x}+\nu_V\left|\frac{\partial^2 u}{\partial x^2}+\frac{\partial^2 u}{\partial y^2}\right|+\frac{\tau_b+\tau_w}{\rho_0}+M_x \tag{16}$$

$$\frac{\partial v}{\partial t}+u\frac{\partial v}{\partial x}+v\frac{\partial v}{\partial y}+fu=-\frac{1}{\rho_0}\frac{\partial p_a}{\partial y}-g\frac{\partial(\zeta-\Delta\zeta)}{\partial y}+\nu_V\left|\frac{\partial^2 v}{\partial x^2}+\frac{\partial^2 v}{\partial y^2}\right|+\frac{\tau_b+\tau_w}{\rho_0}+M_y \tag{17}$$

2.4.3. *Data assimilation scheme for compound flood hazard assessment*

An important aspect of the DA cycle (Fig. 4) is that the variances of input (e.g., initial condition, observation, and BCs) and output data (model states) are assumed to be heteroscedastic, i.e., the variances are proportional to their corresponding magnitudes (Eqs. (6)–(8)). This assumption, in addition to a sufficient ensemble size (*N*), ensures that the ensemble spread can effectively characterize the uncertainty associated with input and output data; hence improving the efficiency of the EnKF technique (Burgers et al., 1998; Moradkhani et al., 2005). In that regard, we tune a set of proportionality factors (*F*) and *N* based on trial-and-error experiments conducted with a high-performance computing system. *F* ranges from 5% to 25% with a 5% increment whereas *N* is set to 25, 50, 100, and 200 members. Based on those experiments, we found that model simulations with 100 ensemble members and factors of initial state and observational data (10%), forcing data (20%), and model states (15%) are suitable for characterizing the associated errors. In addition, we noticed that using a larger *N* (e.g., more than 100 ensemble members) in the DA scheme did not improve the model performance with respect to open-loop (OL) simulations, i.e., simulations where both initial state and forcing data are perturbed without any assimilation cycles. Moreover, we noticed that a larger *N* increased the computational burden and simulation time even with parallel simulations conducted with a high-performance computing

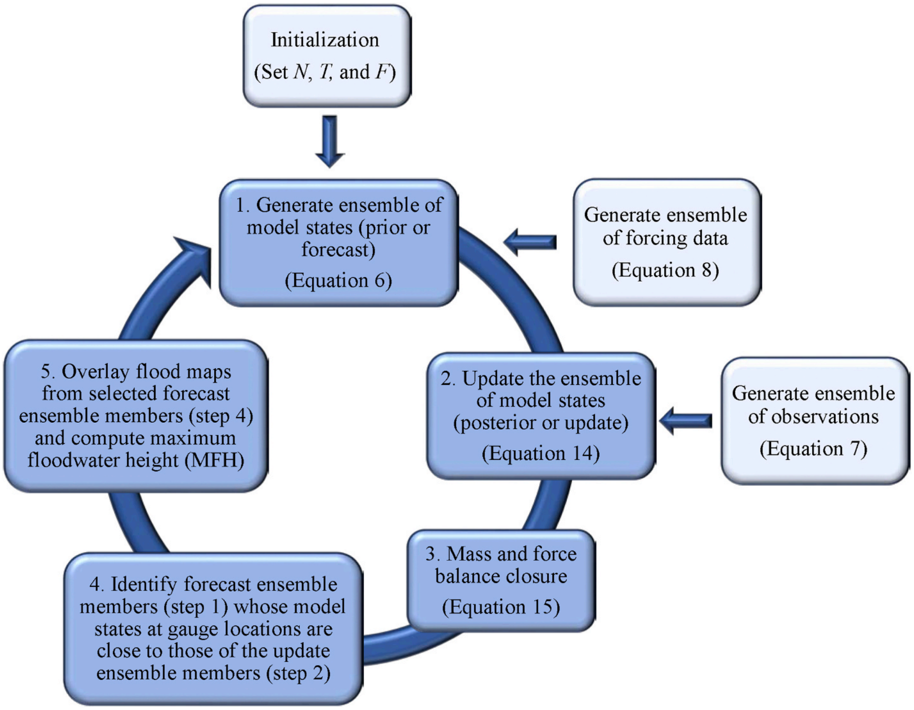

Fig. 4. Schematic of the data assimilation (DA) process with the Ensemble Kalman Filter (EnKF) technique for compound flood hazard assessment (CFHA). Dark-blue boxes are updated sequentially within the DA process. (For interpretation of the references to colour in this figure legend, the reader is referred to the Web version of this article.)

system.

The initial state of the system for every node of the unstructured mesh (Fig. 2) is derived from a 15-day model run prior to the assimilation starting point, which begins on August 20, 2017 and October 26, 2012 for G-Bay and D-Bay, respectively. Likewise, the assimilation cycle is set to 6 h (e.g., WL update every 6h) in accordance to hurricane advisories of the National Hurricane Center. Although daily assimilation cycles are common in hydrological modeling, this would not be useful from a storm surge forecast perspective. The assimilation window encompasses a total time (*T*) of 7 days for D-Bay and 13 days for G-Bay due to a relatively long flood recession period (Fig. S2, supplementary material).

Another key aspect of the DA scheme is the generation of flood hazard maps for CFHA over the study sites. We propose a simple yet practical approach to estimate flood extent and maximum floodwater height (MFH) in absence of readily available satellite imagery for

(a) Galveston Pier 21, TX (NOAA - 8771450)

(b) Lewes, DE (NOAA - 8557380)

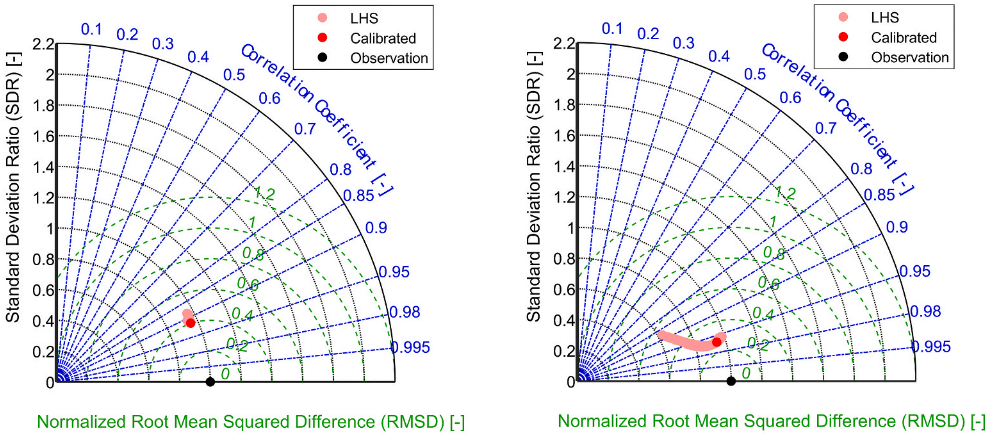

(c) Morgans Point, TX (NOAA - 8770613)

(d) Ship John Shoal, NJ (NOAA - 8537121)

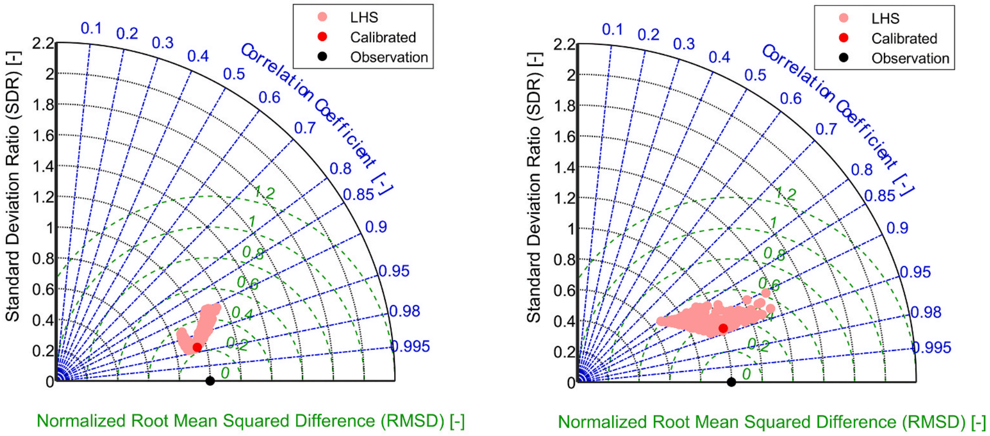

(e) Buffalo Bayou, TX (USGS - 08074710)

(f) Christina River, DE (USGS - 01480120)

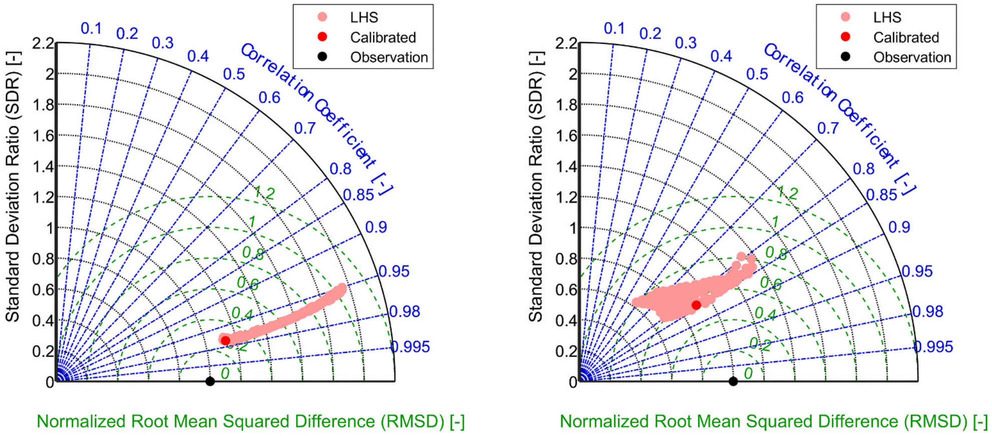

Fig. 5. Taylor diagrams summarizing the goodness of fit between observed and simulated WLs. The statistical metrics evaluate 200 combinations of Manning's roughness values generated using the LHS technique. Selected NOAA and USGS stations represent coastal (a, b), transition (c, d), and upstream areas (e, f) in Galveston Bay (left panel) and Delaware Bay (right panel).

assimilation purposes. The approach consists of identifying ensemble members and their corresponding flood maps that match the WL update at any observation station for a given time step. We argue that these maps preserve the underlying physics controlling compound flood dynamics even though they have not been corrected due to limited observation data in the entire model domain. As part of the identification and/or selection process, we use a threshold value consisting of the desired WL update ±1 cm. The flood maps whose WLs (at the observation stations) fall within the threshold value are then spatially overlayed to compute a single MFH composite for the entire model domain. Note that larger threshold values would eventually identify most of the ensemble members; and consequently, the MFH composite might overestimate floodwater heights instead. The MFH composite is recomputed every 6 h along with WL updates in near real-time, which in turn can assist in flood control management and prompt emergency responses. The proposed approach is further validated with respect to USGS – high water marks collected after Hurricane Harvey and Sandy (Fig. 1).

3. Results and discussion

3.1. Model calibration

We use Taylor diagrams to compare observed and simulated WLs at ten selected NOAA and USGS stations in G-Bay and D-Bay (Fig. 5, and Fig. S1 – supplementary material). Time series used in the diagrams are selected around the peak WL to highlight the models' performance for CF. The pink circles displayed in the Taylor diagrams represent the evaluation metrics obtained from a given combination of Manning's roughness values with respect to observational data (black circle). Among 200 combinations of roughness values, the best combination (red circle) is associated with the calibrated roughness values for all selected stations (Table 1). The statistical metrics of the Taylor diagram suggest that stations located close to the ocean (Fig. 5, top panel) are less sensitive to changes of roughness values as compared to the ones located in transition zones (middle panel) and upstream areas (bottom panel). Consequently, models' performance varies from relatively high accuracies in coastal areas (e.g., RMSD <0.4, SDR close to 1, and $R^2 > 0.9$) to moderate accuracies in upstream areas (e.g., RMSD <0.6, SDR close to 1 and $R^2 > 0.8$).

Moreover, the relative influence of either coastal or inland flood drivers on CF may have affected model's performance at the selected stations despite a robust model calibration with the LHS technique (Fig. S1). CF in G-Bay was characterized by extreme rainfall (7.6×10 m^3) and river-discharge pulses from the Buffalo Bayou River and the San Jacinto River that together produced an excessive freshwater runoff of 1.4×10 m^3 (Huang et al., 2021; Valle-Levinson et al., 2020). The dominance of fluvial flooding over storm surge during Hurricane Harvey probably caused the permanent damage of Lynchburg Landing station (NOAA – 8770733) located at the confluence of those rivers (Valle-Levinson et al., 2020). In contrast, CF in D-Bay was mainly driven by extreme coastal WLs with storm tides of ~1.25 m above mean-higher high water at the Lewes station (Blake et al., 2013). Similarly, the dominance of storm surge over fluvial flooding during Hurricane Sandy may have interrupted the well-functioning of Brandywine Shoal Light station (NOAA - 8555889) located in the lower part of D-Bay (Fanelli et al., 2013).

The evaluation metrics displayed in Fig. S2 (supplementary material) are also calculated around the peak WL. As mentioned before, the models perform satisfactorily at stations located in coastal areas where RMSE is below 0.25 m. Likewise, a relatively high RMSE is observed in transition zones where coastal and inland flood drivers interact. For example, Manchester (Figs. S2–i) and San Jacinto River stations (Figure S2-s) show the strong effect of pluvial and fluvial forcing on G-Bay. Although model simulations match the observed tidal magnitude and phase accurately (NSE >0.87), the model fails in capturing the peak WL attributed to excessive freshwater runoff. G-Bay model overestimates the peak WL by 0.30 m at Manchester station (KGE = 0.85) whereas the peak at San Jacinto River is underestimated by 1.80 m (KGE = 0.68). Similarly, Burlington (Figs. S1–j) and Christina River stations (Fig. S1-t) show the effect of ocean forcing on D-Bay especially at the peak storm surge where the model fails in capturing the peak magnitude even though the tidal phase is correctly represented (NSE >0.74). D-Bay model underestimates the peak WL in both stations with 0.35 m (KGE = 0.69) and 0.40 m (KGE = 0.61), respectively.

This preliminary analysis suggests that hydrodynamic modeling can benefit from DA especially in transition and upstream areas where over- and underestimation of WL are evident regardless of the dominant flood driver (e.g., freshwater runoff or storm surge). Moreover, we argue that a well-calibrated hydrodynamic model may not require correcting time-varying roughness values, unlike hydrological models where model parameters are most often preferred to be corrected in conjunction with model state variables during the assimilation period (Abbaszadeh et al., 2020; Meng et al., 2017; Ziliani et al., 2019). In particular, improvements in hydrodynamic modeling including the underlying physics, mesh decimation, and reliable topobathy data in coastal areas have resulted in a better model skill for storm surge forecasts and CF (Bilskie et al., 2020; Mandli and Dawson, 2014; Santiago-Collazo et al., 2019).

3.2. Data assimilation with the EnKF

The deterministic metrics namely RMSE, NSE, and KGE evaluate the performance of DA (blue text) and OL simulations (red text) at ten NOAA and USGS stations of G-Bay and D-Bay (Fig. 6, and Fig. S3 – supplementary material). In general, the EnKF technique helps reduce both over- and underestimation in WL predictions as compared to the OL simulations; especially in transition and upstream areas where inland and coastal flood drivers interact. In coastal areas (Fig. 6, top panel), such an improvement is noticeable in Galveston Pier 21 station where freshwater runoff attenuates the incoming tide propagating from the Gulf of Mexico. Model simulations after DA can satisfactorily predict WL variability during the CF event since RMSE is reduced by 35% with respect to the OL simulation whereas both NSE and KGE increase up to 0.88. In contrast, the OL simulation overestimates the peak WL including the flood recession limb on August 30. Lewes station in D-Bay shows that WL estimates with DA and OL simulations are almost identical, and tides propagate from the Atlantic Ocean without any noticeable influence of freshwater runoff. Nevertheless, the deterministic metrics reflect a slight improvement in WL prediction with DA since RMSE is reduced by 14% whereas NSE and KGE increase up to 0.96 and 0.95, respectively. Likewise, RL ≥ 0.85 in both stations suggests that the ensemble spread is appropriate for generating reliable WL predictions.

In transition zones (middle panel), Morgans Point shows a moderate improvement in WL prediction. RMSE is reduced by 11% with respect to the OL simulation whereas NSE and KGE increase up to 0.84 and 0.77, respectively. However, after the peak WL on August 27, there is an evident overestimation of WL that propagates over the recession limb. This is likely associated with a high uncertainty in river discharge estimates from the San Jacinto River located at the northeastern side of Houston City (Fig. 1). In fact, detailed analyses of forcing conditions during Hurricane Harvey suggest that the observed WLs at Morgans Point are primarily attributed to the San Jacinto River's flooding with a limited contribution of the Buffalo Bayou River (Valle-Levinson et al., 2020). Similarly, Ship John Shoal station located in the transition zone of D-Bay shows a considerable improvement in WL prediction. The EnKF technique corrects a clear overestimation of high and low WLs on October 30 which in turn helps reduce RMSE by 35% and increase NSE and KGE up to 0.94 and 0.86, respectively. The ensemble spread in both stations can produce reliable WL predictions since RL ≥ 0.90.

The benefit of the EnKF technique for WL prediction is also evident in upstream areas of G-Bay and D-Bay (bottom panel). Buffalo Bayou is among the stations in Houston City that reported historic WLs (>3.5 m) associated with the compound effect of inland and ocean flood drivers.

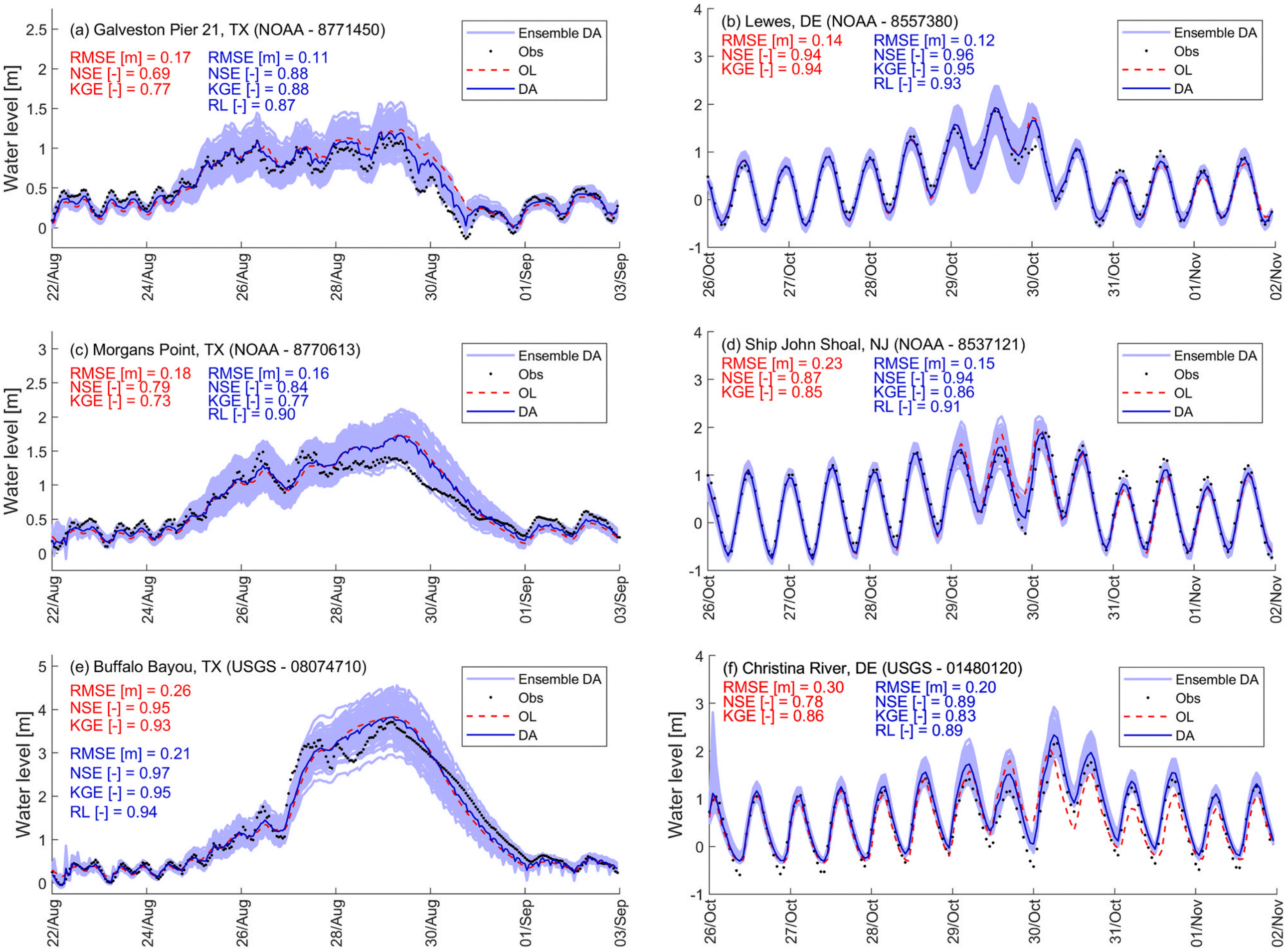

Fig. 6. Predicted and observed WLs using the (EnKF) technique in Galveston Bay (left panel) and Delaware Bay (right panel) for Hurricane Harvey and Hurricane Sandy, respectively. Open-loop (OL) simulations (red dashed lines) and data assimilation (DA) results (blue solid line) are compared to observation data (black dots) in terms of RMSE, NSE, and KGE. The ensemble spread of posterior simulation (light blue) is evaluated with the reliability metric (RL). Selected NOAA and USGS stations represent coastal (a, b), transition (c, d), and upstream areas (e, f). (For interpretation of the references to colour in this figure legend, the reader is referred to the Web version of this article.)

Although both OL and DA simulations match the peak WL, the assimilated one can reproduce WL variability with a higher accuracy especially before August 27. Note that underestimation of WL during the rising limb is compensated by an overestimation around the peak WL on August 28. The latter is reflected in both NSE and KGE as they achieve very high values ranging from 0.93 to 0.97 regardless of the EnKF implementation. Nonetheless, RMSE is reduced by 19% with respect to the OL simulation. Christina River station in D-Bay shows that the OL simulation cannot reproduce WL variability around the peak and beyond August 30. The DA simulation helps reduce both over- and underestimation of WL within the assimilation window, and as a result, RMSE is reduced by 33% with respect to the OL simulation. Likewise, NSE increases up to 0.89 even though KGE shows a slight decrease (0.83) in the DA simulation. RL $\geq$ 0.89 suggests that the ensemble spread is appropriate and can produce reliable WL predictions.

In addition to time series analyses, we compare the prior (forecast) and posterior (update) distributions of WL simulations at NOAA and USGS stations of G-Bay and D-Bay (Fig. 7, and Fig. S4 – supplementary material). In general, the expected value of the posterior distributions is closer to the observed peaks (black circle) than that of the prior distribution in all stations, suggesting that the assimilation process could result in more reliable and accurate WL predictions. In coastal areas (Fig. 7, top panel), such an improvement is more discernible at Galveston Pier 21 station where the EnKF technique helps correct overestimation of WL even at the start of the assimilation process ($t = 0$). This was also observed at the peak WL ($t = tp$) and the end of the simulation period ($t = T$). The improvement of WL prediction is less evident for the Lewes station at the three instances since the calibrated model (OL simulation) can represent storm surge accurately (Fig. 6b). Nevertheless, uncertainty bounds around the observed WL are considerably reduced with the posterior distribution at $t = T$. In transition zones (middle panel), Morgans Point and Ship Jhon Shoal show a similar pattern as the posterior distribution is centered around the observation data and uncertainty is reduced at the three instances. The improvement in WL prediction is also reflected in upstream areas of the study sites (bottom panel). The expected value of prior distributions overestimates the observed WL at Buffalo Bayou station (up to 0.30 m at $t = T$) and underestimates the peak WL at the Christina River station (0.55 m at $t = tp$). Furthermore, note that the prior distribution (WLs before correction or update) tends to overestimate the actual observation in all stations of G-Bay whereas the opposite is observed in D-Bay.

3.3. *Compound flood hazard assessment with DA*

Another key aspect of the DA scheme is the generation of flood hazard maps in the absence of observational data in space (e.g., wetlands, floodplains, etc.) as opposed to gauge (point-based) data. Hereinafer, we compare flood hazard maps obtained from the two well-calibrated models (Fig. S2) with respect to MFH composites derived from the proposed DA scheme (see section 2.4.3). For this, we leverage

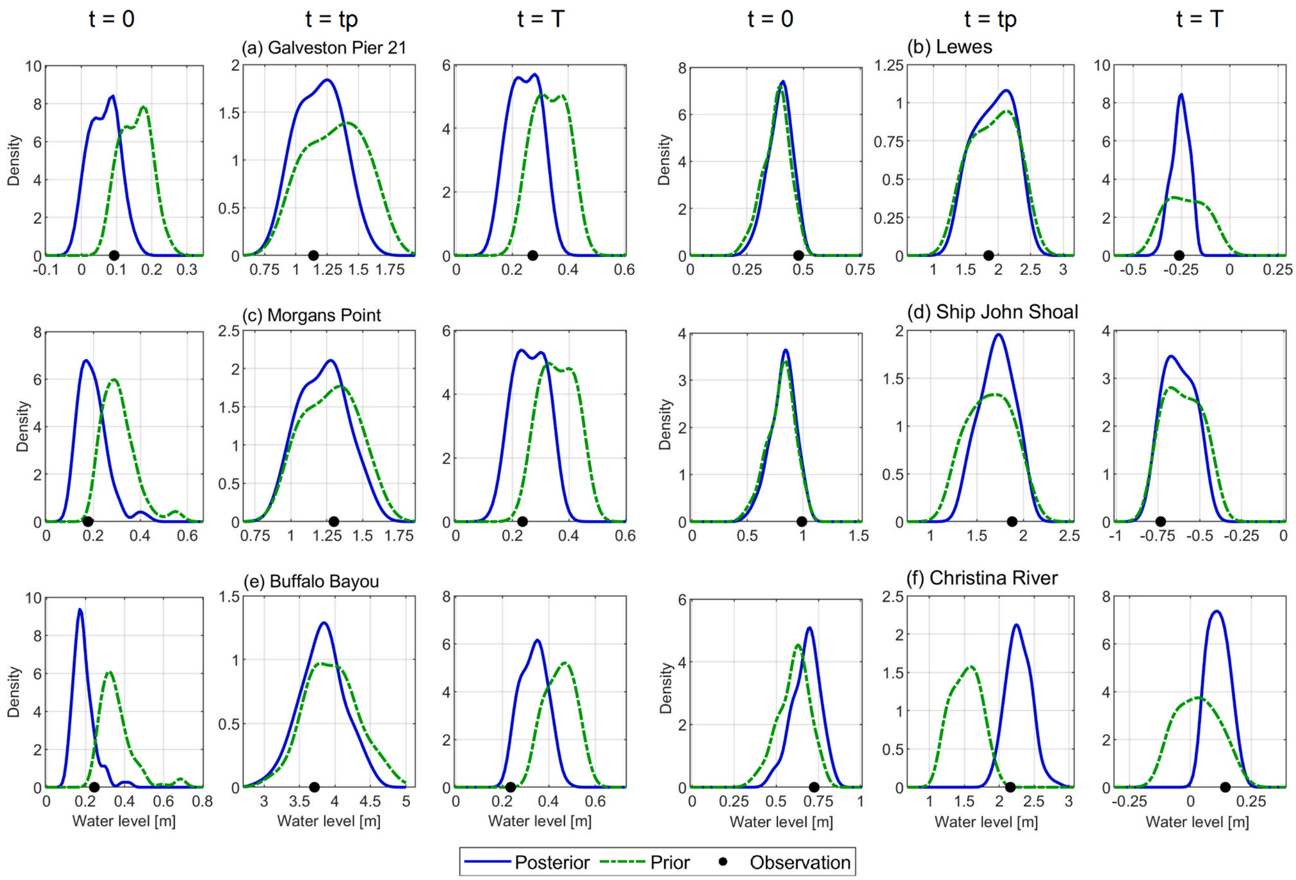

Fig. 7. Forecast (prior) and update (posterior) distributions of WL simulation at the start ($t = 0$), peak WL ($t = tp$), and end of the simulation period ($t = T$) for Galveston Bay (a, c, e) and Delaware Bay (b, d, f). Selected NOAA and USGS stations represent coastal (a, b), transition (c, d), and upstream areas (e, f).

the assimilation process (Fig. 4) and identify flood maps that match the WL update at selected NOAA and USGS stations. These maps are overlayed to compute MFH composites covering the entire model domain. To validate this approach, we compare the resulting composites (and associated point data) with respect to USGS – high water marks collected after Hurricane Harvey and Hurricane Sandy (Fig. 8, top panel). The 1:1 fit line represents a perfect match between simulated and observed maximum WLs in the study sites. In general, the MFH composites are more accurate than flood hazard maps of the well-calibrated models since the mean absolute bias (MAB) is reduced by 25% in G-Bay and by 43% in D-Bay. In both study sites, the calibrated models tend to underestimate the observed high water marks as most of the data is below the 1:1 fit line. In contrast, the MFH composites (or point data) are well aligned with the 1:1 fit line especially in G-Bay that has about 240 verified marks in the model domain (Fig. 1a). Although the MFH composite of D-Bay is validated with only 13 available marks in the model domain (Fig. 1b), the advantage of the DA process is evident as well.

To further examine the benefits of the assimilation process for CFHA, we compare the flood hazard maps andthe MFH composites in terms of WL residuals (Fig. 8, bottom panel). Based on the previous validation process, we consider the MFH composite as a reference and identify zones where flood hazard is overestimated (positive residuals) and underestimated (negative residual). The largest negative residuals are observed along the Buffalo Bayou River (Houston Ship Channel), the San Jacinto River, Cedar Bayou, and surrounding areas where the underestimation of MFH is above 0.7 m. Likewise, MFH is underestimated in the middle of G-Bay (0.6 m) and overestimated in upstream areas beyond the flood risk zone (0.10 m). In contrast, the largest negative residuals in D-Bay are rather scattered around Lewes, Cape May, the Delaware National Estuarine Reserve, and Trenton where the underestimation of MFH is above 1 m. The residual is almost negligible beyond wetland regions (at the edges of the Bay) and in upstream areas of D-Bay.

Overall, the DA process via the EnKF technique allows for reducing uncertainty in CFHA as compared to a rigorously calibrated model. Although assimilation of flood extent from satellite-based imagery (or radar data) is desirable (Annis et al., 2021), this is not always possible from a CFHA perspective. Satellite's revisit frequency is usually in the order of days, and so hinders sequential assimilation of spatial data and/or near real-time flood detection and mapping (Anusha and Bharathi, 2020; Kabir et al., 2020; Muñoz et al., 2021b; Uddin et al., 2019). Moreover, even with available cloud-free imagery and/or radar data, the acquisition date may not coincide with that of the maximum flood extent and so hinder any efforts in CFHA with DA. Our approach attempts to overcome this issue by generating near real-time MFH composites within the DA cycle (6 h-update).

4. Conclusions

Compound flood hazard assessment (CFHA) is a challenging yet crucial task that can benefit from data assimilation (DA) techniques. Although coastal hydrodynamic models are well-suited to predict storm surge and associated WL variability, complex and nonlinear interactions emerging from inland and coastal flood drivers increase the uncertainty in WL prediction and compound flood modeling especially in coastal to inland transition zones. In this study, we first developed a pair of high-resolution hydrodynamic models in Delft3D-FM, corrected wetland elevation bias in topographic data, and conducted a robust model calibration with the Latin hypercube sampling (LHS) technique in order to reduce any potential source of error in WL and compound flood simulations. We then used a DA scheme based on the Ensemble Kalman Filter

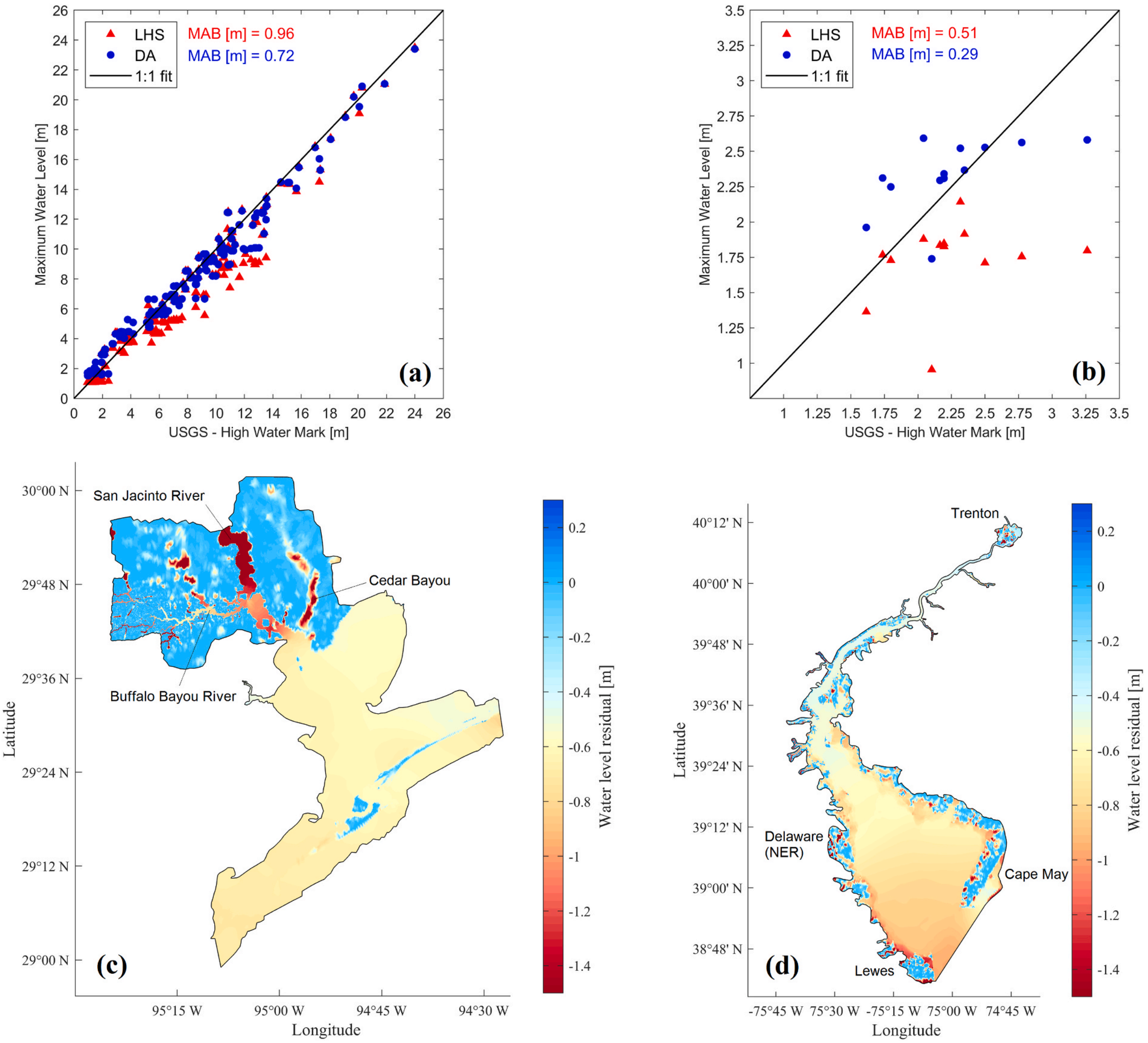

Fig. 8. Compound flood hazard assessment (CFHA) for Hurricane Harvey in Galveston Bay (left panel) and Hurricane Sandy in Delaware Bay (right panel). (a, b) Validation of maximum floodwater height composites (MFH) with respect to high water marks of the U.S. Geological Survey (USGS). (c, d) WL residuals between flood hazard maps of well-calibrated models (based on LHS) and MFH composites (based on DA) show zones of overestimation (positive) and underestimation (negative) when conducting CFHA.

(EnKF) technique and hydrodynamic modeling to provide reliable WL predictions and accurate near real-time flood hazard maps (e.g., 6 h-sequential update). We selected the EnKF technique to correct model states (WL estimates) in coastal to inland transition zones since the ensemble-based formulation is suitable for systems with strongly nonlinear dynamics (Evensen, 2002); especially those emerging from complex interactions of pluvial, fluvial, and ocean drivers. In addition, we attempted to close the mass and force balance of the system by adjusting both continuity and momentum equations and so forced the system to the desired surface WL. The proposed DA scheme was tested on two well-known compound flood events and study sites in the United States, namely Hurricane Harvey for Galveston Bay (G-Bay) and Hurricane Sandy for Delaware Bay (D-Bay), and further validated with verified high water marks of the U.S. Geological Survey.

Compound flooding (CF) in G-Bay was primarily attributed to extreme freshwater runoff from the San Jacinto River and the Buffalo Bayou River that jointly elevated WLs in both inland and coastal gauge stations. For this event, the proposed DA scheme corrected overestimation in WL predictions (up to 0.25 m) with respect to open-loop simulations and reduced mean absolute bias (MAB) by 25% with respect to the calibrated model. Unlike the G-Bay, CF in D-Bay was driven by extreme coastal WLs (storm surge) that propagated from the ocean boundary to inland stations distributed along the Delaware River. Here, the DA scheme corrected underestimation in the predictions (up to 0.55 m) and reduced MAB by 43%. From a CFHA perspective, the assimilation process helped generate maximum floodwater height (MFH) composites as a proxy for updated WLs over the entire model domain (e.g., flood hazard maps). The composites preserved the underlying physics of CF and were additionally conditioned to match WL updates at available gauge stations. The near real-time MFH composites allowed the identification of over- and underestimation zones when conducting CFHA with/out assimilation of WL. We conclude that even a rigorously calibrated model can benefit from DA regardless of the dominant flood driver in CF. Future research is advisable towards more advanced DA techniques, mainly the Particle Filtering (Abbaszadeh et al., 2018, 2019; Moradkhani et al., 2018), for CFHA to overcome inherent limitations of the EnKF technique such as linear updating rule, Gaussian assumption of errors in observations, and mass and force balance closure. The DA scheme proposed here can help generate actionable flood risk information on a near-real time basis and so assist decision makers and emergency responders in case of compound coastal flooding (i.e. hurricanes).

Credit author statement

Muñoz David F.: Conceptualization, Methodology, Software, Validation, Formal analysis, Writing – original draft, Visualization. Abbaszadeh Peyman.: Methodology, Formal analysis, Writing – review & editing. Moftakhari Hamed.: Conceptualization, Writing – review & editing, Supervision, Funding acquisition. Moradkhani Hamid.: Methodology, Writing – review & editing, Supervision, Funding acquisition.

Declaration of competing interest

The authors declare that they have no known competing financial interests or personal relationships that could have appeared to influence the work reported in this paper.

Acknowledgments

This study is partially funded by the National Science Foundation INFEWS Program (award EAR-1856054). Also, partial support was provided by USACE contract #W912HZ2020055.

Appendix

Table A.1
Summary of evaluation metrics used for compound flood hazard assessment with data assimilation.

Evaluation metrics	Equation
Pearson's correlation	$R^2 = \frac{1}{T-1}\sum_{t=1}^{T}\left(\frac{o_t - u_o}{\sigma_o}\right)\left(\frac{s_t - u_s}{\sigma_s}\right) = \frac{cov(o_t, s_t)}{\sigma_o \sigma_s}$
Centered root mean square difference	$RMSD = \left\{\frac{1}{T}\sum_{t=1}^{T}\left[(s_t - u_s) - (o_t - u_o)\right]^2\right\}^{1/2}$
Standard deviation ratio	$SDR = \frac{\sigma_s}{\sigma_o}$
Nash-Sutcliffe efficiency	$NSE = 1 - \frac{\sum_{t=1}^{T}(s_t - o_t)^2}{\sum_{t=1}^{T}(o_t - u_o)^2}$
Kling-Gupta efficiency	$KGE = 1 - \left\{\left[\frac{cov(o_t, s_t)}{\sigma_o \sigma_s} - 1\right]^2 + \left[\left(\frac{\sigma_s}{\sigma_o}\right) - 1\right]^2 + \left[\left(\frac{u_s}{u_o}\right) - 1\right]^2\right\}^{1/2}$
Mean absolute bias	$MAB = \frac{1}{T}\sum_{t=1}^{T}\lvert s_t - o_t\rvert$
Reliability	$RL = 1 - 2\sum_{i=1}^{N}\left\lvert p_{x(i)} - p_{x(i)}^{(th)}\right\rvert$

Where *t*: time step, *T*: total time steps, o_t: observation data, s_t: model simulation, u_o: mean of observation data, u_s: mean of model simulations, σ_o: standard deviation of observation data, σ_u: standard deviation of model simulations, *cov*: covariance, *N*: ensemble size, *x*: ensemble member, $p_{x(i)}$: *i*th observed *p*-value, and ${p_{x(i)}}^{(th)}$: theoretical *p*-value of *x* at *t*.

Appendix A. Supplementary data

Supplementary data to this article can be found online at https://doi.org/10.1016/j.coastaleng.2021.104057.

References

Abbaszadeh, P., Gavahi, K., Moradkhani, H., 2020. Multivariate remotely sensed and in-situ data assimilation for enhancing community WRF-Hydro model forecasting. Adv. Water Resour. 145, 103721 https://doi.org/10.1016/j.advwatres.2020.103721.

Abbaszadeh, P., Moradkhani, H., Daescu, D.N., 2019. The quest for model uncertainty quantification: a hybrid ensemble and variational data assimilation framework. Water Resour. Res. 55, 2407–2431. https://doi.org/10.1029/2018WR023629.

Abbaszadeh, P., Moradkhani, H., Yan, H., 2018. Enhancing hydrologic data assimilation by evolutionary Particle Filter and Markov chain Monte Carlo. Adv. Water Resour. 111, 192–204. https://doi.org/10.1016/j.advwatres.2017.11.011.

AghaKouchak, A., Huning, L.S., Chiang, F., Sadegh, M., Vahedifard, F., Mazdiyasni, O., Moftakhari, H., Mallakpour, I., 2018. How do natural hazards cascade to cause disasters? Nature 561, 458–460. https://doi.org/10.1038/d41586-018-06783-6.

Alizad, K., Hagen, S.C., Medeiros, S.C., Bilskie, M.V., Morris, J.T., Balthis, L., Buckel, C. A., 2018. Dynamic responses and implications to coastal wetlands and the surrounding regions under sea level rise. PLoS One 13, e0205176. https://doi.org/10.1371/journal.pone.0205176.

Annis, A., Nardi, F., Castelli, F., 2021. Simultaneous assimilation of water levels from river gauges and satellite flood maps for near-real time flood mapping. Hydrol. Earth Syst. Sci. Discuss. 2021, 1–37. https://doi.org/10.5194/hess-2021-125.

Anusha, N., Bharathi, B., 2020. Flood detection and flood mapping using multi-temporal synthetic aperture radar and optical data. The Egyptian Journal of Remote Sensing and Space Science 23, 207–219. https://doi.org/10.1016/j.ejrs.2019.01.001.

Arcement, G.J., Schneider, V.R., 1989. Guide for Selecting Manning's Roughness Coefficients for Natural Channels and Flood Plains. US Government Printing Office, Washington, DC.

Asher, T.G., Luettich Jr., R.A., Fleming, J.G., Blanton, B.O., 2019. Low frequency water level correction in storm surge models using data assimilation. Ocean Model. 144, 101483 https://doi.org/10.1016/j.ocemod.2019.101483.

Bakhtyar, R., Maitaria, K., Velissariou, P., Trimble, B., Mashriqui, H., Moghimi, S., Abdolali, A., Westhuysen, A.J.V. der, Ma, Z., Clark, E.P., Flowers, T., 2020. A New 1D/2D coupled modeling approach for a riverine-estuarine system under storm events: application to Delaware river basin. J. Geophys. Res.: Oceans 125, e2019JC015822. https://doi.org/10.1029/2019JC015822.

Bensi, M., Mohammadi, S., Kao, S.-C., DeNeale, S.T., 2020. Multi-Mechanism Flood Hazard Assessment: Critical Review of Current Practice and Approaches. https://doi.org/10.2172/1637939. No. ORNL/TM-2020/1447). Oak Ridge National Lab. (ORNL), Oak Ridge, TN (United States).

Bertino, L., Evensen, G., Wackernagel, H., 2003. Sequential data assimilation techniques in oceanography. Int. Stat. Rev. 71, 223–241. https://doi.org/10.1111/j.1751-5823.2003.tb00194.x.

Bevacqua, Maraun, D., Vousdoukas, M.I., Voukouvalas, E., Vrac, M., Mentaschi, L., Widmann, M., 2019. Higher probability of compound flooding from precipitation and storm surge in Europe under anthropogenic climate change. Science Advances 5. https://doi.org/10.1126/sciadv.aaw5531 eaaw5531.

Bilskie, M.V., Hagen, S.C., 2018. Defining flood zone transitions in low-gradient coastal regions. Geophys. Res. Lett. 45, 2761–2770. https://doi.org/10.1002/2018GL077524.

Bilskie, M.V., Hagen, S.C., 2013. Topographic accuracy assessment of bare earth lidar-derived unstructured meshes. Adv. Water Resour. 52, 165–177. https://doi.org/10.1016/j.advwatres.2012.09.003.

Bilskie, M.V., Hagen, S.C., Medeiros, S.C., 2020. Unstructured finite element mesh decimation for real-time Hurricane storm surge forecasting. Coast. Eng. 156, 103622 https://doi.org/10.1016/j.coastaleng.2019.103622.

Blake, E., Kimberlain, T., Berg, R., Cangialosi, J., Beven II, J., 2013. Hurricane Sandy, national hurricane center. Tropical cyclone report (AL182012). https://www.nhc.noaa.gov/data/tcr/AL182012_Sandy.pdf, 2012.

Blake, E., Zelinsky, D., 2018. Hurricane Harvey, national hurricane center, tropical cyclone report (AL092017). https://www.nhc.noaa.gov/data/tcr/AL092017_Harvey.pdf.

Burgers, G., Leeuwen, P.J. van, Evensen, G., 1998. Analysis scheme in the ensemble kalman filter. Mon. Weather Rev. 126, 1719–1724. https://doi.org/10.1175/1520-0493(1998)126<1719:ASITEK>2.0.CO;2.

Cañizares, R., Heemink, A.W., Vested, H.J., 1998. Application of advanced data assimilation methods for the initialisation of storm surge models. J. Hydraul. Res. 36, 655–674. https://doi.org/10.1080/00221689809498614.

Cea, L., French, J.R., 2012. Bathymetric error estimation for the calibration and validation of estuarine hydrodynamic models. Estuarine, Coastal and Shelf Science, Recent advances in biogeochemistry of coastal seas and continental shelves 100, 124–132. https://doi.org/10.1016/j.ecss.2012.01.004.

Chow, V.T., 1959. Open-channel Hydraulics. McGraw-Hill civil engineering series.

DeChant, C.M., Moradkhani, H., 2012. Examining the effectiveness and robustness of sequential data assimilation methods for quantification of uncertainty in hydrologic forecasting. Water Resour. Res. 48 https://doi.org/10.1029/2011WR011011.

Deltares, 2021. Delft3D flexible mesh suite - deltares [WWW document]. Delft3D flexible mesh suite. https://www.deltares.nl/en/software/delft3d-flexible-mesh-suite/ (accessed 11.21.19).

Evensen, G., 2002. Sequential data assimilation for nonlinear dynamics: the ensemble kalman filter. In: Pinardi, N., Woods, J. (Eds.), Ocean Forecasting: Conceptual Basis and Applications. Springer, Berlin, Heidelberg, pp. 97–116. https://doi.org/10.1007/978-3-662-22648-3_6.

Fanelli, C., Fanelli, P., Wolcott, D., 2013. Hurricane Sandy - Report of the National Oceanic and Atmospheric Administration.

Gallien, N., Delisle, M.-P.C., Tang, B.-X., Lucey, J.T.D., Winters, M.A., 2018. Coastal flood modeling challenges in defended urban backshores. Geosciences 8, 450. https://doi.org/10.3390/geosciences8120450.

Ghanbari, M., Arabi, M., Kao, S.-C., Obeysekera, J., Sweet, W., 2021. Climate change and changes in compound coastal-riverine flooding hazard along the U.S. Coasts. Earth's Future 9, e2021EF002055. https://doi.org/10.1029/2021EF002055.

Ghil, M., Malanotte-Rizzoli, P., 1991. Data assimilation in meteorology and oceanography. In: Dmowska, R., Saltzman, B. (Eds.), Advances in Geophysics. Elsevier, pp. 141–266. https://doi.org/10.1016/S0065-2687(08)60442-2.

Gupta, H.V., Kling, H., Yilmaz, K.K., Martinez, G.F., 2009. Decomposition of the mean squared error and NSE performance criteria: implications for improving hydrological modelling. J. Hydrol. 377, 80–91. https://doi.org/10.1016/j.jhydrol.2009.08.003.

Hasan Tanim, A., Goharian, E., 2021. Developing a hybrid modeling and multivariate analysis framework for storm surge and runoff interactions in urban coastal flooding. J. Hydrol. 595, 125670 https://doi.org/10.1016/j.jhydrol.2020.125670.

Heemink, A.W., 1986. Storm surge prediction using Kalman filtering. Rijkswaterstaat Commun. 46 (Also Dissertation TU Twente).

Helton, J.C., Davis, F.J., 2003. Latin hypercube sampling and the propagation of uncertainty in analyses of complex systems. Reliab. Eng. Syst. Saf. 81, 23–69. https://doi.org/10.1016/S0951-8320(03)00058-9.

Hendry, A., Haigh, I.D., Nicholls, R.J., Winter, H., Neal, R., Wahl, T., Joly-Laugel, A., Darby, S.E., 2019. Assessing the characteristics and drivers of compound flooding events around the UK coast. Hydrol. Earth Syst. Sci. 23, 3117–3139. https://doi.org/10.5194/hess-23-3117-2019.

Houtekamer, P.L., Zhang, F., 2016. Review of the ensemble kalman filter for atmospheric data assimilation. Mon. Weather Rev. 144, 4489–4532. https://doi.org/10.1175/MWR-D-15-0440.1.

Huang, W., Ye, F., Zhang, Y.J., Park, K., Du, J., Moghimi, S., Myers, E., Pe'eri, S., Calzada, J.R., Yu, H.C., Nunez, K., Liu, Z., 2021. Compounding factors for extreme flooding around Galveston bay during hurricane Harvey. Ocean Model. 158, 101735 https://doi.org/10.1016/j.ocemod.2020.101735.

Iman, R.L., Helton, J.C., Campbell, J.E., 1981. An approach to sensitivity analysis of computer models: Part I—introduction, input variable selection and preliminary variable assessment. J. Qual. Technol. 13, 174–183.

Joyce, J., Chang, N.-B., Harji, R., Ruppert, T., Singhofen, P., 2018. Cascade impact of hurricane movement, storm tidal surge, sea level rise and precipitation variability on flood assessment in a coastal urban watershed. Clim. Dynam. 51, 383–409. https://doi.org/10.1007/s00382-017-3930-4.

Kabir, S., Patidar, S., Xia, X., Liang, Q., Neal, J., Pender, G., 2020. A deep convolutional neural network model for rapid prediction of fluvial flood inundation. J. Hydrol. 590, 125481 https://doi.org/10.1016/j.jhydrol.2020.125481.

Kalman, R.E., 1960. A New approach to linear filtering and prediction problems. J. Basic Eng 82, 35–45. https://doi.org/10.1115/1.3662552.

Klerk, W.J., Winsemius, H.C., van Verseveld, W.J., Bakker, A.M.R., Diermanse, F.L.M., 2015. The co-incidence of storm surges and extreme discharges within the Rhine–Meuse Delta. Environ. Res. Lett. 10, 035005 https://doi.org/10.1088/1748-9326/10/3/035005.

Kulp, S.A., Strauss, B.H., 2019. New elevation data triple estimates of global vulnerability to sea-level rise and coastal flooding. Nat. Commun. 10, 4844. https://doi.org/10.1038/s41467-019-12808-z.

Leonard, M., Westra, S., Phatak, A., Lambert, M., Hurk, B. van den, McInnes, K., Risbey, J., Schuster, S., Jakob, D., Stafford-Smith, M., 2014. A compound event framework for understanding extreme impacts. Wiley Interdisciplinary Reviews: Climate Change 5, 113–128. https://doi.org/10.1002/wcc.252.

Lesser, G.R., Roelvink, J.A., Kester, J.A.T.M. van, Stelling, G.S., 2004. Development and validation of a three-dimensional morphological model. Coast. Eng. 51, 883–915. https://doi.org/10.1016/j.coastaleng.2004.07.014.

Liu, Z., Merwade, V., Jafarzadegan, K., 2018. Investigating the role of model structure and surface roughness in generating flood inundation extents using one- and two-dimensional hydraulic models. Journal of Flood Risk Management, e12347. https://doi.org/10.1111/jfr3.12347, 0.

Madsen, Cañizares, R., 1999. Comparison of extended and ensemble Kalman filters for data assimilation in coastal area modelling. Int. J. Numer. Methods Fluid. 31, 961–981. https://doi.org/10.1002/(SICI)1097-0363(19991130)31:6<961::AID-FLD907>3.0.CO;2-0.

Mandli, K.T., Dawson, C.N., 2014. Adaptive mesh refinement for storm surge. Ocean Model. 75, 36–50. https://doi.org/10.1016/j.ocemod.2014.01.002.

Matgen, P., Montanari, M., Hostache, R., Pfister, L., Hoffmann, L., Plaza, D., Pauwels, V.R.N., De Lannoy, G.J.M., De Keyser, R., Savenije, H.H.G., 2010. Towards the sequential assimilation of SAR-derived water stages into hydraulic models using the Particle Filter: proof of concept. Hydrol. Earth Syst. Sci. 14, 1773–1785. https://doi.org/10.5194/hess-14-1773-2010.

Mayo, T., Butler, T., Dawson, C., Hoteit, I., 2014. Data assimilation within the Advanced Circulation (ADCIRC) modeling framework for the estimation of Manning's friction coefficient. Ocean Model. 76, 43–58. https://doi.org/10.1016/j.ocemod.2014.01.001.

Medeiros, S., Hagen, S., Weishampel, J., Angelo, J., 2015. Adjusting lidar-derived digital terrain models in coastal marshes based on estimated aboveground biomass density. Rem. Sens. 7, 3507–3525. https://doi.org/10.3390/rs70403507.

Meng, S., Xie, X., Liang, S., 2017. Assimilation of soil moisture and streamflow observations to improve flood forecasting with considering runoff routing lags. J. Hydrol. 550, 568–579. https://doi.org/10.1016/j.jhydrol.2017.05.024.

Moftakhari, H., Salvadori, G, AghaKouchak, A., Sanders, B.F., Matthew, R.A., 2017. Compounding effects of sea level rise and fluvial flooding. Proc. Natl. Acad. Sci. Unit. States Am. 114, 9785–9790. https://doi.org/10.1073/pnas.1620325114.

Moftakhari, Schubert, J.E., AghaKouchak, A., Matthew, R.A., Sanders, B.F., 2019. Linking statistical and hydrodynamic modeling for compound flood hazard assessment in tidal channels and estuaries. Adv. Water Resour. 128, 28–38. https://doi.org/10.1016/j.advwatres.2019.04.009.

Moradkhani, H., 2008. Hydrologic remote sensing and land surface data assimilation. Sensors 8, 2986–3004. https://doi.org/10.3390/s8052986.

Moradkhani, H., Nearing, G., Abbaszadeh, P., Pathiraja, S., 2018. Fundamentals of data assimilation and theoretical advances. In: Duan, Q., Pappenberger, F., Thielen, J., Wood, A., Cloke, H.L., Schaake, J.C. (Eds.), Handbook of Hydrometeorological Ensemble Forecasting. Springer, Berlin, Heidelberg, pp. 1–26. https://doi.org/10.1007/978-3-642-40457-3_30-1.

Moradkhani, H., Sorooshian, S., Gupta, H.V., Houser, P.R., 2005. Dual state–parameter estimation of hydrological models using ensemble Kalman filter. Adv. Water Resour. 28, 135–147. https://doi.org/10.1016/j.advwatres.2004.09.002.

Morton, R.A., Barras, J.A., 2011. Hurricane impacts on coastal wetlands: a half-century record of storm-generated features from southern Louisiana. coas 27, 27–43. https://doi.org/10.2112/JCOASTRES-D-10-00185.1.

Muis, S., Lin, N., Verlaan, M., Winsemius, H.C., Ward, P.J., Aerts, J.C.J.H., 2019. Spatiotemporal patterns of extreme sea levels along the western North-Atlantic coasts. Sci. Rep. 9, 3391. https://doi.org/10.1038/s41598-019-40157-w.

Muñoz, D.F., Cissell, J.R., Moftakhari, H., 2019. Adjusting emergent herbaceous wetland elevation with object-based image analysis, random forest and the 2016 NLCD. Rem. Sens. 11, 2346. https://doi.org/10.3390/rs11202346.

Muñoz, D.F., Moftakhari, H., Moradkhani, H., 2020. Compound effects of flood drivers and wetland elevation correction on coastal flood hazard assessment. Water Resour. Res. 56, e2020WR027544 https://doi.org/10.1029/2020WR027544.

Muñoz, Muñoz, P., Alipour, A., Moftakhari, H., Moradkhani, H., Mortazavi, B., 2021a. Fusing multisource data to estimate the effects of urbanization, sea level rise, and hurricane impacts on long-term wetland change dynamics. IEEE Journal of Selected Topics in Applied Earth Observations and Remote Sensing 14, 1768–1782. https://doi.org/10.1109/JSTARS.2020.3048724.

Muñoz, Muñoz, P., Moftakhari, H., Moradkhani, H., 2021b. From local to regional compound flood mapping with deep learning and data fusion techniques. Sci. Total Environ. 782, 146927 https://doi.org/10.1016/j.scitotenv.2021.146927.

Nash, J.E., Sutcliffe, J.V., 1970. River flow forecasting through conceptual models part I — a discussion of principles. J. Hydrol. 10, 282–290. https://doi.org/10.1016/0022-1694(70)90255-6.

Nasr, A.A., Wahl, T., Rashid, M.M., Camus, P., Haigh, I.D., 2021. Assessing the dependence structure between oceanographic, fluvial, and pluvial flooding drivers along the United States coastline. Hydrol. Earth Syst. Sci. Discuss. 1–31. https://doi.org/10.5194/hess-2021-268.

Navon, I.M., 2009. Data assimilation for numerical weather prediction: a review. In: Park, S.K., Xu, L. (Eds.), Data Assimilation for Atmospheric, Oceanic and Hydrologic Applications. Springer, Berlin, Heidelberg, pp. 21–65. https://doi.org/10.1007/978-3-540-71056-1_2.

Nearing, G.S., Tian, Y., Gupta, H.V., Clark, M.P., Harrison, K.W., Weijs, S.V., 2016. A philosophical basis for hydrological uncertainty. Hydrol. Sci. J. 61, 1666–1678. https://doi.org/10.1080/02626667.2016.1183009.

NOAA-NHC, 2020. National hurricane center [WWW Document]. URL. https://www.nhc.noaa.gov/ (accessed 1.16.20).

Parodi, M.U., Giardino, A., van Dongeren, A., Pearson, S.G., Bricker, J.D., Reniers, A.J.H.M., 2020. Uncertainties in coastal flood risk assessments in small island developing states. Nat. Hazards Earth Syst. Sci. 20, 2397–2414. https://doi.org/10.5194/nhess-20-2397-2020.

Pathiraja, S., Moradkhani, H., Marshall, L., Sharma, A., Geenens, G., 2018. Data-driven model uncertainty estimation in hydrologic data assimilation. Water Resour. Res. 54, 1252–1280. https://doi.org/10.1002/2018WR022627.

Potapov, P., Hansen, M.C., Kommareddy, I., Kommareddy, A., Turubanova, S., Pickens, A., Adusei, B., Tyukavina, A., Ying, Q., 2020. Landsat analysis ready data for global land cover and land cover change mapping. Rem. Sens. 12, 426. https://doi.org/10.3390/rs12030426.

Pugh, D., Woodworth, P., 2014. Sea-level Science: Understanding Tides, Surges, Tsunamis and Mean Sea-Level Changes. Cambridge University Press.

Renard, B., Kavetski, D., Kuczera, G., Thyer, M., Franks, S.W., 2010. Understanding predictive uncertainty in hydrologic modeling: the challenge of identifying input and structural errors. Water Resour. Res. 46 https://doi.org/10.1029/2009WR008328.

Roelvink, J.A., Van Banning, G., 1995. Design and development of DELFT3D and application to coastal morphodynamics. Oceanogr. Lit. Rev. 11, 925.

Sadegh, M., Moftakhari, H., Gupta, H.V., Ragno, E., Mazdiyasni, O., Sanders, B., Matthew, R., AghaKouchak, A., 2018. Multihazard scenarios for analysis of compound extreme events. Geophys. Res. Lett. 45, 5470–5480. https://doi.org/10.1029/2018GL077317.

Saleh, F., Ramaswamy, V., Wang, Y., Georgas, N., Blumberg, A., Pullen, J., 2017. A multi-scale ensemble-based framework for forecasting compound coastal-riverine flooding: the Hackensack-Passaic watershed and Newark Bay. Adv. Water Resour. 110, 371–386. https://doi.org/10.1016/j.advwatres.2017.10.026.

Salehi, M., 2018. Storm surge and wave impact of low-probability hurricanes on the lower Delaware bay—calibration and application. J. Mar. Sci. Eng. 6, 54. https://doi.org/10.3390/jmse6020054.

Salvadori, G., Durante, F., Michele, C.D., Bernardi, M., Petrella, L., 2016. A multivariate copula-based framework for dealing with hazard scenarios and failure probabilities. Water Resour. Res. 52, 3701–3721. https://doi.org/10.1002/2015WR017225.

Sanders, B.F., Schubert, J.E., 2019. PRIMo: parallel raster inundation model. Adv. Water Resour. 126, 79–95. https://doi.org/10.1016/j.advwatres.2019.02.007.

Sanders, B.F., Schubert, J.E., Goodrich, K.A., Houston, D., Feldman, D.L., Basolo, V., Luke, A., Boudreau, D., Karlin, B., Cheung, W., Contreras, S., Reyes, A., Eguiarte, A., Serrano, K., Allaire, M., Moftakhari, H., AghaKouchak, A., Matthew, R.A., 2020. Collaborative modeling with fine-resolution data enhances flood awareness, minimizes differences in flood perception, and produces actionable flood maps. Earth's Future 8, e2019EF001391. https://doi.org/10.1029/2019EF001391.

Santiago-Collazo, F.L., Bilskie, M.V., Hagen, S.C., 2019. A comprehensive review of compound inundation models in low-gradient coastal watersheds. Environ. Model. Software 119, 166–181. https://doi.org/10.1016/j.envsoft.2019.06.002.

Sebastian, A., Gori, A., Blessing, R.B., Wiel, K. van der, Bass, B., 2019. Disentangling the impacts of human and environmental change on catchment response during Hurricane Harvey. Environ. Res. Lett. 14, 124023 https://doi.org/10.1088/1748-9326/ab5234.

Sebastian, A., Proft, J., Dietrich, J.C., Du, W., Bedient, P.B., Dawson, C.N., 2014. Characterizing hurricane storm surge behavior in Galveston Bay using the SWAN+ADCIRC model. Coast. Eng. 88, 171–181. https://doi.org/10.1016/j.coastaleng.2014.03.002.

Serafin, K.A., Ruggiero, P., Parker, K., Hill, D.F., 2019. What's streamflow got to do with it? A probabilistic simulation of the competing oceanographic and fluvial processes driving extreme along-river water levels. Nat. Hazards Earth Syst. Sci. 19, 1415–1431. https://doi.org/10.5194/nhess-19-1415-2019.

Taylor, K.E., 2001. Summarizing multiple aspects of model performance in a single diagram. J. Geophys. Res.: Atmosphere 106, 7183–7192. https://doi.org/10.1029/2000JD900719.

Uddin, K., Matin, M.A., Meyer, F.J., 2019. Operational flood mapping using multi-temporal sentinel-1 SAR images: a case study from Bangladesh. Rem. Sens. 11, 1581. https://doi.org/10.3390/rs11131581.

USGS, 2011. Discharge measurement quality code — USGS water data for the nation help system [WWW document]. https://help.waterdata.usgs.gov/codes-and-parameters/discharge-measurement-quality-code (accessed 5.3.21).

Valle-Levinson, A., 2010. Contemporary Issues in Estuarine Physics. Cambridge University Press.

Valle-Levinson, A., Olabarrieta, M., Heilman, L., 2020. Compound flooding in houston-Galveston bay during hurricane Harvey. Sci. Total Environ. 747, 141272 https://doi.org/10.1016/j.scitotenv.2020.141272.

Verlaan, M., Heemink, A.W., 1997. Tidal flow forecasting using reduced rank square root filters. Stoch. Hydrol. Hydraul. 11, 349–368. https://doi.org/10.1007/BF02427924.

Wahl, T., Haigh, I.D., Nicholls, R.J., Arns, A., Dangendorf, S., Hinkel, J., Slangen, A.B.A., 2017. Understanding extreme sea levels for broad-scale coastal impact and adaptation analysis. Nat. Commun. 8, 16075. https://doi.org/10.1038/ncomms16075.

Wahl, T., Jain, S., Bender, J., Meyers, S.D., Luther, M.E., 2015. Increasing risk of compound flooding from storm surge and rainfall for major US cities. Nat. Clim. Change 5, 1093–1097. https://doi.org/10.1038/nclimate2736.

Ward, P.J., Couasnon, A., Eilander, D., Haigh, I.D., Hendry, A., Muis, S., Veldkamp, T.I.E., Winsemius, H.C., Wahl, T., 2018. Dependence between high sea-level and high river discharge increases flood hazard in global deltas and estuaries. Environ. Res. Lett. 13, 084012 https://doi.org/10.1088/1748-9326/aad400.

Wechsler, S.P., 2007. Uncertainties associated with digital elevation models for hydrologic applications: a review. Hydrol. Earth Syst. Sci. Discuss. 11, 1481–1500.

Whitney, M.M., Garvine, R.W., 2006. Simulating the Delaware bay buoyant outflow: comparison with observations. J. Phys. Oceanogr. 36, 3–21. https://doi.org/10.1175/JPO2805.1.

Wu, W, Emerton, R, Duan, Q, Wood, A.W., Wetterhall, F, Robertson, D.E., et al., 2020. Ensemble flood forecasting: current status and future opportunities. Wires Water 7 (3). https://doi.org/10.1002/wat2.1432.

Ye, F., Huang, W., Zhang, Y.J., Moghimi, S., Myers, E., Pe'eri, S., Yu, H.-C., 2021. A cross-scale study for compound flooding processes during Hurricane Florence. Nat. Hazards Earth Syst. Sci. 21, 1703–1719. https://doi.org/10.5194/nhess-21-1703-2021.

Ye, F., Zhang, Y.J., Yu, H., Sun, W., Moghimi, S., Myers, E., Nunez, K., Zhang, R., Wang, H.V., Roland, A., Martins, K., Bertin, X., Du, J., Liu, Z., 2020. Simulating storm surge and compound flooding events with a creek-to-ocean model: importance of baroclinic effects. Ocean Model. 145, 101526 https://doi.org/10.1016/j.ocemod.2019.101526.

Ziliani, M.G., Ghostine, R., Ait-El-Fquih, B., McCabe, M.F., Hoteit, I., 2019. Enhanced flood forecasting through ensemble data assimilation and joint state-parameter estimation. J. Hydrol. 577, 123924 https://doi.org/10.1016/j.jhydrol.2019.123924.

Zscheischler, J., Martius, O., Westra, S., Bevacqua, E., Raymond, C., Horton, R.M., van den Hurk, B., AghaKouchak, A., Jézéquel, A., Mahecha, M.D., Maraun, D., Ramos, A.M., Ridder, N.N., Thiery, W., Vignotto, E., 2020. A typology of compound weather and climate events. Nature Reviews Earth & Environment 1, 333–347. https://doi.org/10.1038/s43017-020-0060-z.